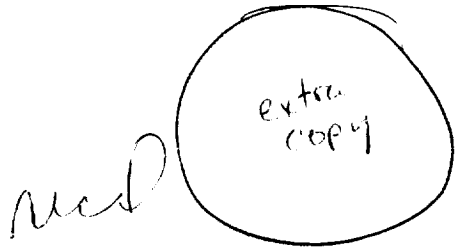

Material Characterization for Ductile Fracture Prediction

Final Report on UC Davis - NASA
Interchange NCC-2-5214

December, 2000

Michael R. Hill

Mechanical and Aeronautical Engineering
University of California, Davis
One Shields Avenue
Davis, CA 95616

ABSTRACT

The research summarized in this document provides valuable information for structural health evaluation of NASA infrastructure. Specifically, material properties are reported which will enable calibration of ductile fracture prediction methods for three high-toughness metallic materials and one aluminum alloy which can be found in various NASA facilities. The task of investigating these materials has also served to validate an overall methodology for ductile fracture prediction is currently being employed at NASA. In facilitating the ability to incorporate various materials into the prediction scheme, we have provided data to enable demonstration of the overall generality of the approach.

Table of Contents

List of Figures

Original Research Statement

Objective

The goal of this research is to extend the methodology for structural assessment of aging infrastructure developed by NASA-Ames, Code JEE. The research proposed herein will extend the methodology by measuring material properties and calibrating micromechanical failure models for three high-toughness metallic materials of interest NASA-wide. In pursuing the application of this methodology to additional materials, this project will also demonstrate the generality of the overall approach.

Background

Welded Pressure Systems

Several of NASA's missions require the containment of highly-pressurized gas. Large volumes of compressed gas in aerodynamic test facilities at Ames Research Center, for example, contain dangerous levels of potential energy. The successful containment of pressurized gasses is mandatory for both Center function and for safety. Risk management for such pressure systems often involves the use of code-sanctioned construction, inspection, and operation practices. But, because of the age of many NASA facilities, this is a difficult task. Many older systems have exhausted their initial design lifetime, mandating system re-certification.

Changes in various code requirements has made re-certification a vastly different process than the initial operational certification following construction. This is especially true for many of Ames larger facilities which were fabricated from high-toughness steels using welded construction. For these facilities, the re-certification process is complicated by several factors, including the elastic-plastic nature of the fracture process and welding residual stresses. In response to these difficulties, a methodology has been developed by NASA-Ames Code JEE for structural assessment, including the prediction of fatigue and fracture in welded structures.

Progress at NASA Ames

To date, Ames' program on pressure system safety has been successful in addressing several aspects of structural health assessment in aging welded structures. Progress has been made on residual stress measurement in welded joints[1], fatigue crack growth prediction in the presence of residual stress[2], ductile and brittle fracture prediction in high-toughness metals[3], and fracture prediction in the presence of residual stress.[4] Ames is now focused on further verification of its methodology and application to additional materials of interest NASA-wide.

1. Hill, M. R. and D. V. Nelson (1996). "Determination of Residual Stress Based on the Estimation of Eigenstrain." NASA Ames Research Center, Final Report on Interchange No. NCC2–879.
2. Hill, M. R. and D. V. Nelson (1995). "Internal Weld Defects: Residual Stress Fields and Effect on Fatigue Lifetime." NASA Ames Research Center, Final Report on Interchange No. NCA2-767.
3. Panontin, T. L. (1994). The Relationship Between Constraint and Ductile Fracture Initiation as Defined by Micromechanical Analyses. Stanford University.

Extension of the Methodology to Additional Materials

Much of the proposed assessment methodology is based on testing and examination of high-toughness materials used in Ames' ground-based systems. NASA-wide other, similar, materials are in use in aerospace systems, including 304 and 17-4 stainless steel, and Inconel 718. Since the fracture methodology developed at Ames is general in its approach, structures composed of other materials can, in principle, be analyzed within the same framework. However, the efficacy of the proposed methodology with respect to each material has not been examined. We, therefore, propose to investigate the extension of the ductile fracture prediction portion of Ames' overall methodology to these three additional materials, SS304, SS17-4, and Inconel 718.

Proposed Approach

In order to investigate the ductile fracture process, Ames has employed a framework which combines computational mechanics with micromechanical theories of fracture. The computational aspect involves highly detailed finite element modeling of a cracked geometry of interest. The goal of modeling is to determine the stress and plastic strain fields in the vicinity of the crack-tip and their evolution with loading. Such modeling requires both a sound finite element model, with a well-refined mesh, and an accurate description of the material stress-strain response. With both of these entities available, crack-tip stress and strain can be estimated for a given material and geometry by using non-linear elastic-plastic finite element analysis. Given the crack-tip stress and strain history, micromechanical theories are then employed to arrive at estimates of fracture load. Therefore, to predict ductile fracture in a given material, a stress-strain curve must be determined and each micromechanical theory must be properly calibrated.

Determination of Flow Properties

The prediction of ductile fracture requires the stress-strain behavior of a given material to be defined up to large values of plastic strain. This will be accomplished by using a slightly waisted tensile specimen, as shown in Figure 1. The waist of this specimen allows the monitoring of diametral contraction during the test, up to the point of final ductile fracture, by attachment of a diametral extensometer. Since diametral contraction is measured, the area of the specimen after necking can be determined at any point during the test and the true stress versus logarithmic strain history computed, which is required for non-linear analysis.

4. Panontin, T. L. and M. R. Hill (1997). "The effect of residual stresses on brittle and ductile fracture initiation predicted by micromechanical models." International Journal of Fracture (to appear).

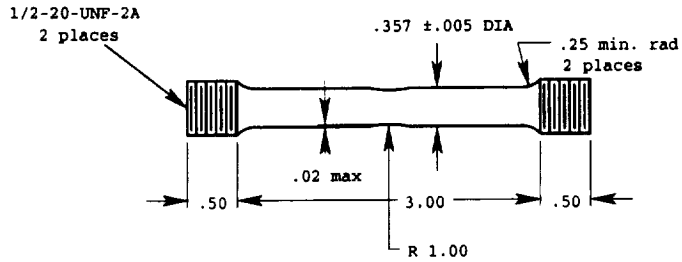

Figure 1 – *Waisted tensile specimen used to determine the stress strain curve to large plastic strain.*

Calibration of the Initiation Model

Further tensile testing will also be performed to calibrate micromechanical ductile fracture initiation criteria. In the computational mechanics, J_2 plasticity theory is employed to predict plastic flow. This model predicts plastic flow at some level of deviatoric stress, regardless of the amount of hydrostatic stress present. Conversely, micromechanical models of fracture depend on both the deviatoric and hydrostatic stresses attending the fracture process. Two additional tensile specimens, shown in Figure 2, will be used to investigate the point of ductile fracture initiation. These two specimens, referred to as notched-tensile specimens, each have a differing notch radius which together provide two combinations of hydrostatic and deviatoric stress. Micromechanical models of ductile fracture predict final failure in these specimens at different local stress and strain. The stress state present at the fracture load will therefore be used to calibrate parameters in the ductile fracture failure criterion for a given material, including initial porosity and characteristic distance. Consequently, testing of both tensile and notched-tensile specimens allows the determination of the material flow curve and calibration of the ductile fracture initiation criteria.

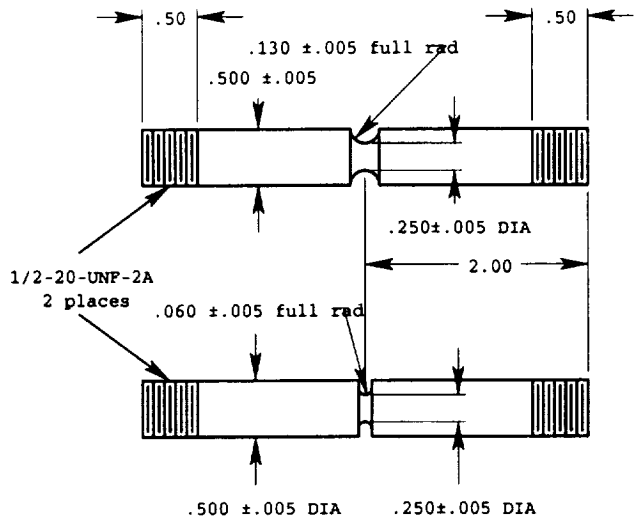

Figure 2 – *Waisted tensile specimen used to determine the stress strain curve to large plastic strain.*

Calibration of the Tearing Model

To calibrate micromechanical models of the ductile tearing process, elastic-plastic modeling and fracture testing will be performed using a standard ~~compact tension (CT)~~ single edge notched bending (SEB) geometry for each material. As when calibrating the initiation criteria, modeling will provide the stress and strain history in the vicinity of the crack-tip and tearing criteria will be invoked to estimate the amount of ductile crack extension (tearing) under increasing load. Physical ~~CT~~ SEB specimens will be tested to estimate the *J*-R curve for each material (which is directly related to the load vs. crack extension curve), in compliance with ASTM E1152-87. The results of physical fracture testing, together with the numerical modeling, will allow calibration of the parameters within the micromechanical ductile tearing model.

Summary of Accomplishments

1) Tensile testing of the following materials and specimens.

Table 1: Materials and specimens tensile tested

Material	Waisted	Large notch	Medium notch	Small notch
S17400	x	x	x	
N07718 (annealed)	x	x	x	
N07718 (STA-1)	x	x	x	
S30400	x	x	x	
A07050 (T7451)	x	x	x	x

2) Flow curve generation for elastic-plastic finite element modeling of S17400, N07718 (annealed), N07718 (STA-1), S30400, and A07050 (T7451).
3) Mesh generation for companion finite element modeling of the following materials and specimens

Table 2: Finite element meshes generated for companion modeling

Material	Waisted	Large notch	Medium notch	Small notch	SE(B)
S17400	x	x	x		x
N07718 (STA-1)	x	x	x		x
N07718 (annealed)	x	x	x		x
S30400	x	x	x		x
A07050 (T7451)	x	x	x	x	x

4) Elastic-plastic finite element analysis of the following materials and specimens.

Table 3: Materials and specimens tensile tested

Material	Waisted	Large notch	Medium notch	Small notch	SE(B)
S17400	x	x	x		
N07718 (annealed)	x	x	x		
N07718 (STA-1)	x	x	x		
S30400	x	x	x		
A07050 (T7451)	x	x	x	x	x

5) Single edge cracked bend (SE(B)) *R*-curve tests of the following materials and specimens.

Table 4: Materials and specimens fracture tested (nominal dimensions, inches)

Material	Width (W)	Thickness (B)	Span (S)	Initial crack (a_o/W)
S17400	2.0	1.0	8.0	0.5
N07718 (annealed)	1.5	0.75	6.0	0.5
N07718 (STA-1)	1.5	0.75	6.0	0.5
S30400	2.5	1.25	10	0.5
A07050 (T7451)	1.0	0.5	4.0	0.5 and 0.15

6) Residual stress measurements in 7050 (T7451) plate
7) Micromechanical calibration of 7050 (T7451) using the SMCS methodology

Results from Tensile Specimens

The range of tensile specimens tested is shown in Figure 3.

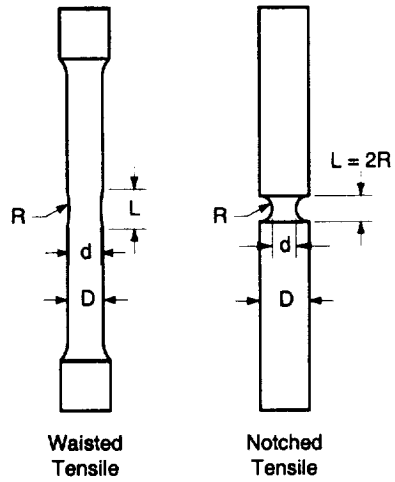

Figure 3 – *Waisted and notched tensile specimens. Dimensions in Table 5*

Table 5: Tensile specimen dimensions (refer to Figure 3, above).

Designation	D, mm (inch)	d, mm (inch)	R, mm (inch)
Waisted	9.2 (0.362)	8.2 (0.322)	25.4 (1.0)
Large Notch	12.7 (0.5)	6.4 (0.25)	3.2 (0.125)
Medium Notch	12.7 (0.5)	6.4 (0.25)	1.6 (0.062)
Small Notch	12.7 (0.5)	6.4 (0.25)	1.0 (0.040)

Mechanical Properties

Mechanical properties resulting from testing of waisted samples are reported in Table 6 below, together with data obtained from references (mostly ASM data) and certification documents. Data gathered during the all tensile tests included load, axial extension, and diametral strain. These data were used to obtain an initial estimate of the true stress, log strain flow curve for each material. Companion modeling was used to obtain a more accurate flow curve, accounting for the triaxial state of stress in the specimen neck. Companion modeling was also used to determine the stress and strain state in the specimens at the point of fracture.

Table 6: Measured material properties with data from references.

		Reference		*Certification*				
Material	**Condition**	**E (Mpsi)**	**ν**	**Sy (ksi)**	**Su (ksi)**	**%RA**	**% e**	**Hardness**
S17400	H900	28.50	0.27	175.70	198.60	40.30	13.50	415 BHN
	H1150							
N07718	Mill annealed			73.00	124.00			99 RB
	Aged	31.80	0.31	182.00	199.00			44 RC
S30400	Annealed	29.00	0.27	37.80	89.30	78.00	58.40	152 BHN
A07050	T7451	10.40	0.33	70.50	79.00		11.00	
				Experiment				
Material	**Condition**			**Sy (ksi)**	**Su (ksi)**	**%RA**	**% e**	**Hardness**
S17400	As received			140.00	157.00	47.10		
N07718	As received			56.00	125.20	52.10		
	STA-1			169.00	196.00	54.90		
S30400	As received			51.00	100.70	74.90		
A07050	T7451			77.00	83.90	21.70		

Modeling of Tensile Specimens

Finite element modeling was used obtain a flow curve for each material. Typical meshes are shown in Figure 4. They exploit the axisymmetry of the cylindrical geometries and symmetry about the center of the specimen length. Refinement was increased to obtain a converged solution.

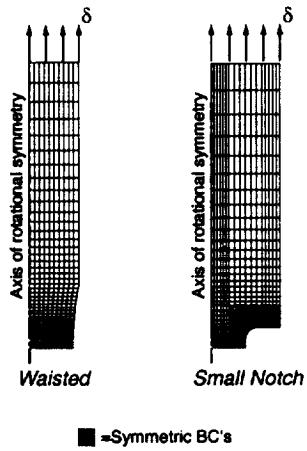

Figure 4 – *Finite element meshes for tensile specimens.*

Flow Properties (true stress, log strain curves)

Engineering stress and diametral strain measurements from waisted specimens were coupled with axisymmetric finite element analyses to obtain true-stress, logarithmic strain flow curves that could be used in future elastic-plastic modeling of these materials. In all cases, measured data were used to formulate an initial flow curve. Then the flow curve was changed to achieve a match between measured and computed trajectories of engineering stress versus diametral strain. The final trajectories are shown to the right of each flow curve. The format of the flow curves below are as required by the ABAQUS finite element software (each line is a pair of true stress (in psi) and logarithmic plastic strain).

S17400

```
*ELASTIC
28.5E6,0.27
*PLASTIC
75000.000, 0.0000000
122000.000, 0.0016828
134000.000, 0.0068766
138000.000, 0.0186140
159000.000, 0.0821207
163000.000, 0.1129000
168500.000, 0.1957083
180000.000, 0.5787557
```

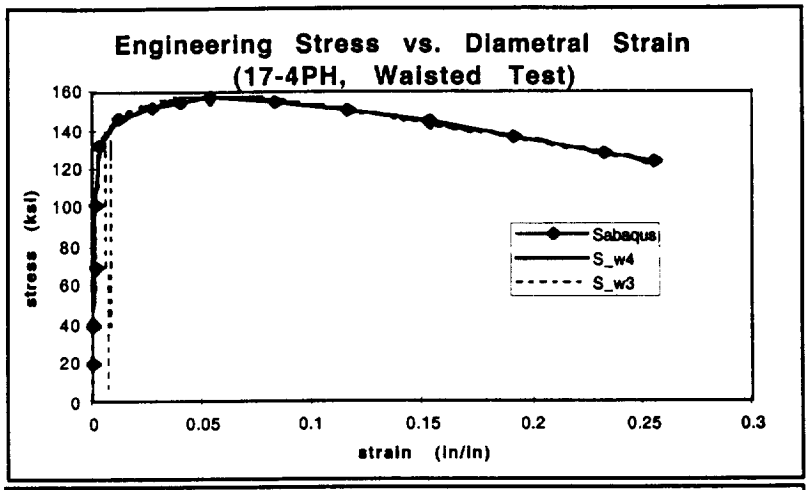

N07718 (as received)

```
*ELASTIC
31.8E6,0.306
*PLASTIC
52488.962, 0.0000000
62000.000, 0.0143480
73000.000, 0.0391340
83200.000, 0.0672300
97000.000, 0.1036494
121598.436, 0.1803855
139500.000, 0.2356000
166000.000, 0.3399576
186000.000, 0.4373000
196000.000, 0.5439659
205000.000, 0.7065227
```

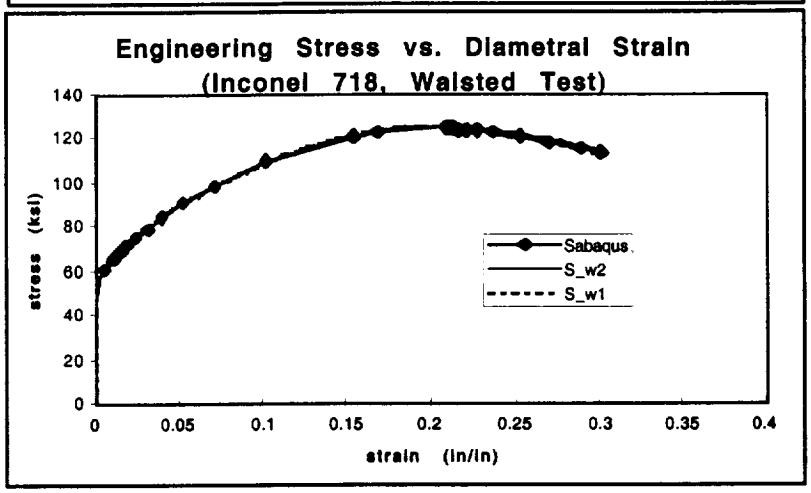

N07718 (STA-1)

```
*ELASTIC
31.8E6,0.306
*PLASTIC
150000.0, 0.00000
152000.0, 0.00100
154000.0, 0.00200
155000.0, 0.00350
159000.0, 0.01000
165000.0, 0.02000
176000.0, 0.04000
183000.0, 0.06000
196000.0, 0.10000
212000.0, 0.15000
218000.0, 0.17500
224000.0, 0.20000
235000.0, 0.25000
244000.0, 0.30000
256000.0, 0.40000
264000.0, 0.50000
```

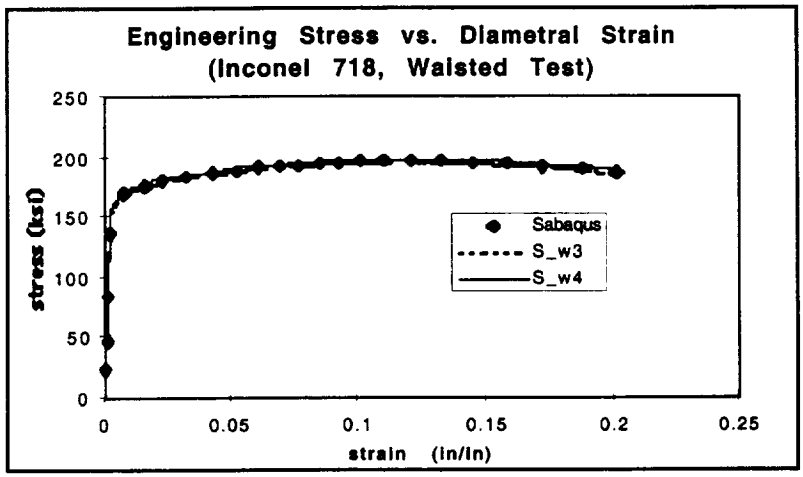

S30400

```
*ELASTIC
29.E6,0.27
*PLASTIC
42055.870, 0.0000000
55000.000, 0.0204840
63000.000, 0.0388792
112000.000, 0.2570000
142000.000, 0.4011952
165000.000, 0.5512809
179000.000, 0.6662346
199000.000, 0.8813428
217000.000, 1.1168901
234000.000, 1.4347234
```

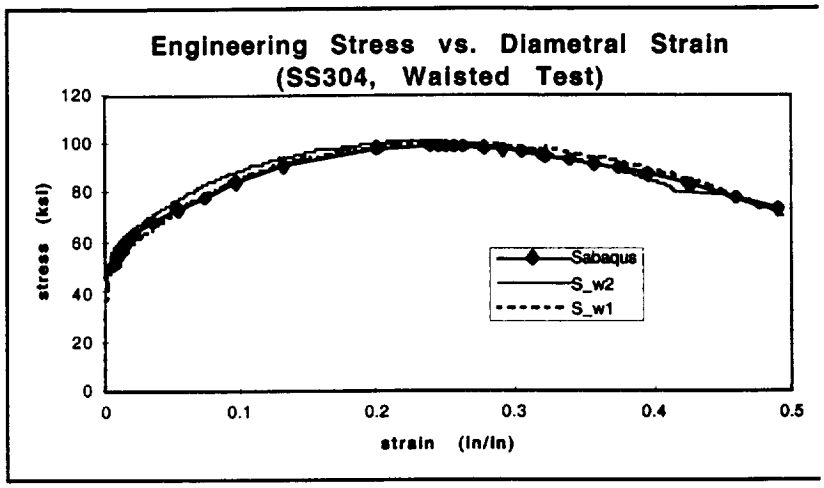

A07050

```
*ELASTIC
10.4E6,0.330
*PLASTIC
59104.762,0
68628.571,0.0016828
73390.476,0.0149
81600.000,0.0522
85100.000,0.0821207
86700.000,0.1129
88200.000,0.18
88700.000,0.2568
```

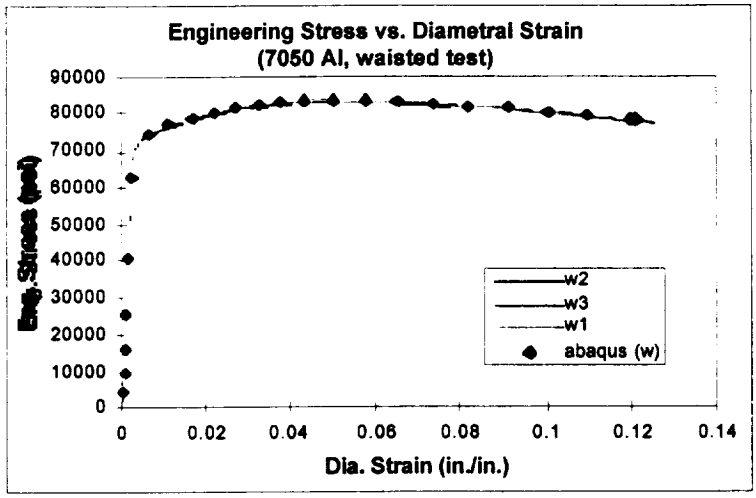

Stress and Strain at Failure of Tensile Specimens

Companion modeling of tensile specimens provided data on the influence of constraint on plastic strain to failure in these materials. Modelling employed the meshes and flow curves presented above for the range of specimens tested in the study. Trajectories of measured and computed engineering stress versus diametral strain were used to determine the point of failure in the computation. Example results are shown in Figure 5. The final point on the FEM trajectory of this figure is defined as failure, and corresponds to the average point of fracture in the replicate specimens for each geometry.

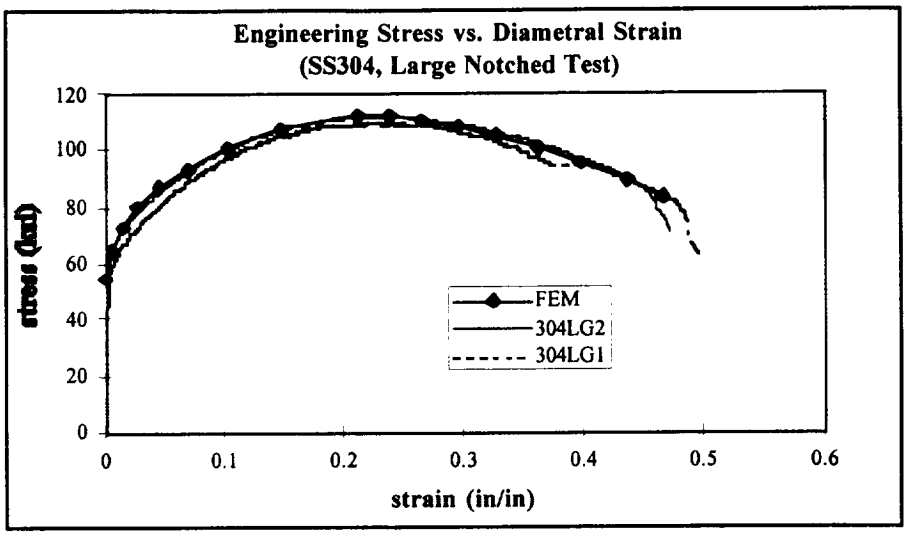

Figure 5 – *Experimental and computational results for large notch tensile testing in S30400*

At this failure point, the stress and strain for each specimen is characterized by the equivalent plastic strain and stress triaxiality at the center of each specimen. Results for all specimens and materials are shown below. These results provide the basis for calibration of various micromechanical models.

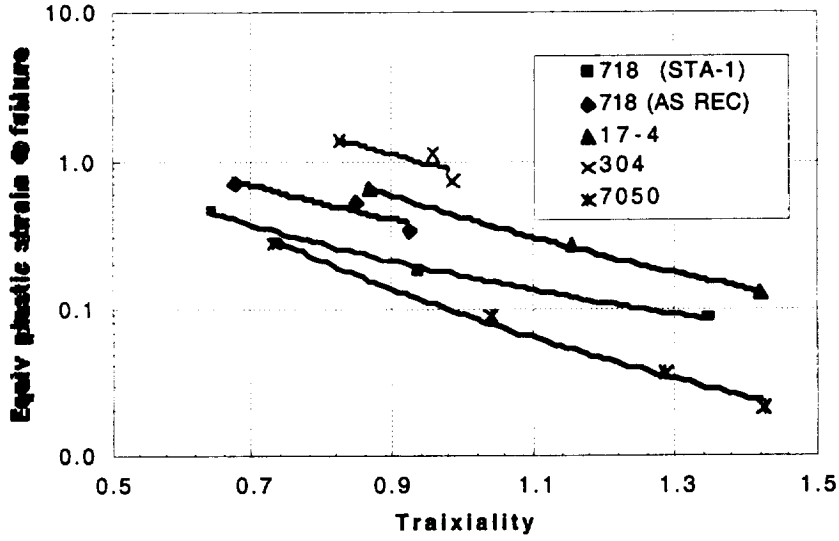

Figure 6 – *Stress and strain state at failure of tensile specimens in all materials.*

Results from Fracture Specimens

Fracture Toughness

Fracture testing followed ASTM E1152 and ASTM E813 and used SE(B) specimens.

Specimen sizes were given in Table 4, above, and were adequate to obtain measurements of J_{IC} according to E813, except in the case of annealed 718. The annealed 304 did not exhibit tearing behavior in the SE(B) testing, and follow-up C(T) tests were conducted at Ames; however, these results are not available. Fracture toughness results for the remaining materials, averaged over replicate specimens, are shown in Table 7.

Table 7: Measured values of fracture toughness J_{IC}

Material	J_{IC} (lb/in)
S17400	340
N07718 (annealed)	4760[a]
N07718 (STA-1)	1715
S30400	--
A07050 (T7451)	83.3

a. Size requirements of E813 not satisfied.

J-integral - Resistance Curves

Measured *J-R* curves are shown in Figures 7 through 13.

S17400

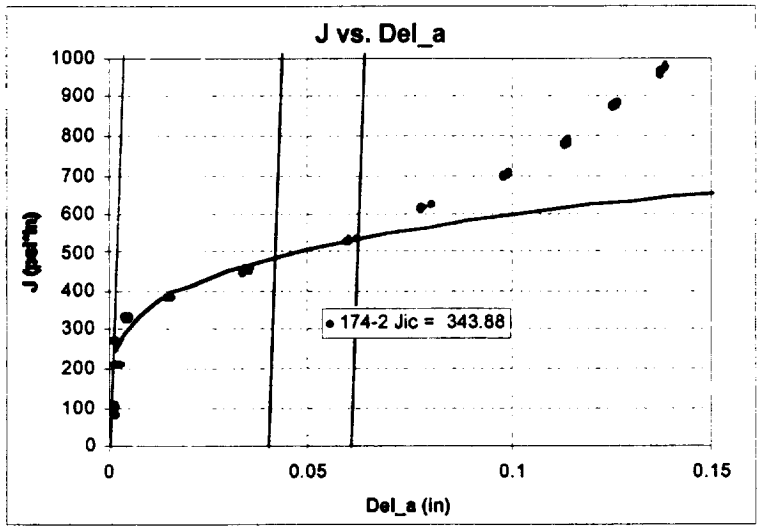

Figure 7 – *Fracture test results for specimen 174-2*

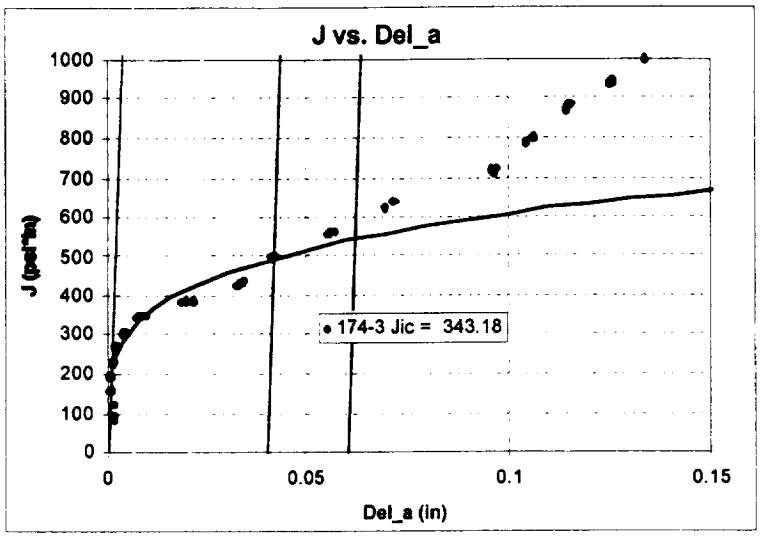

Figure 8 – *Fracture test results for specimen 174-3*

N07718 (as received, toughness exceeds size requirements)

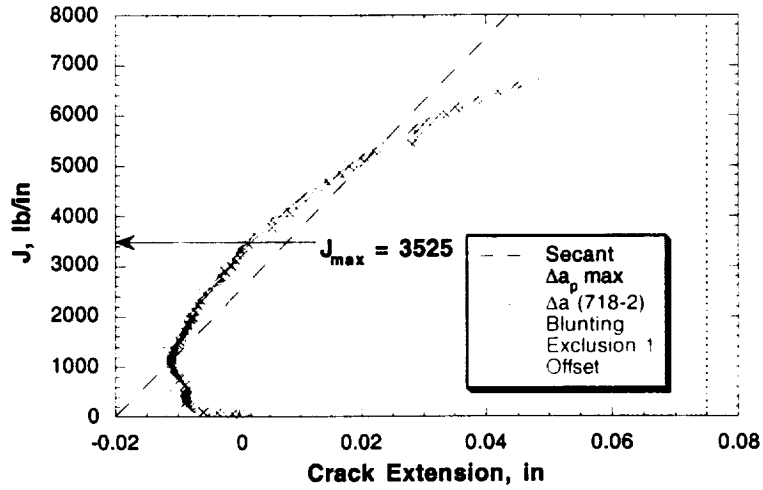

Figure 9 – *Fracture test results for specimen 718-2*

N07718 (STA-1)

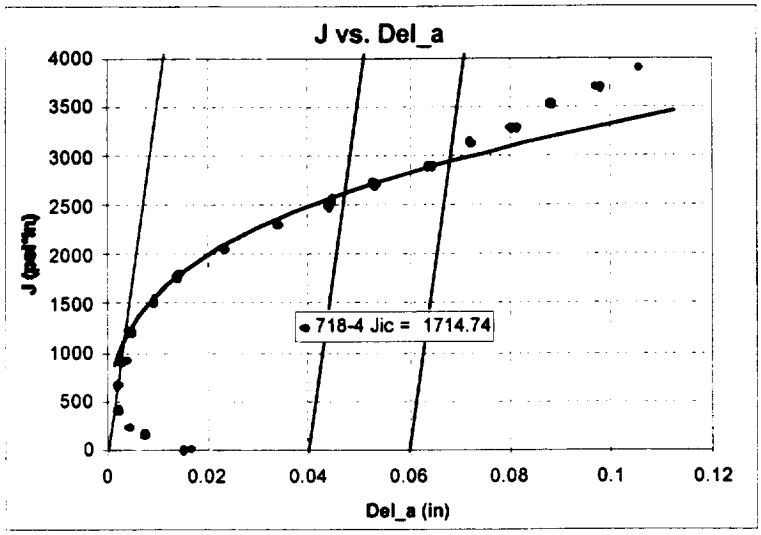

Figure 10 – *Fracture test results for specimen 718-4 (heat treated)*

S30400 (no tearing observed)

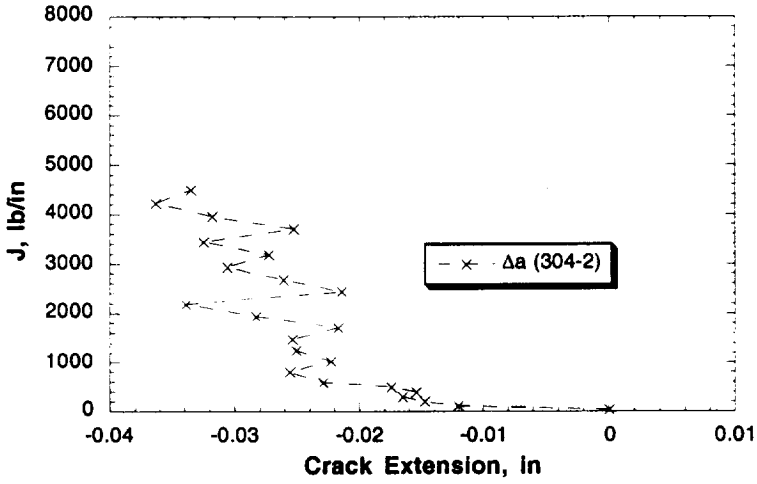

Figure 11 – *Fracture test results for specimen 304-2*

A07050 (T7451)

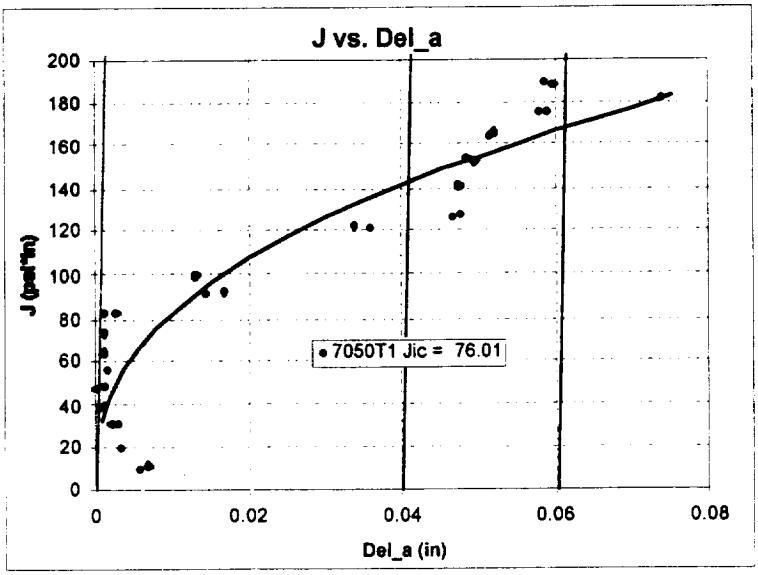

Figure 12 – *Fracture test results for specimen 7050T1*

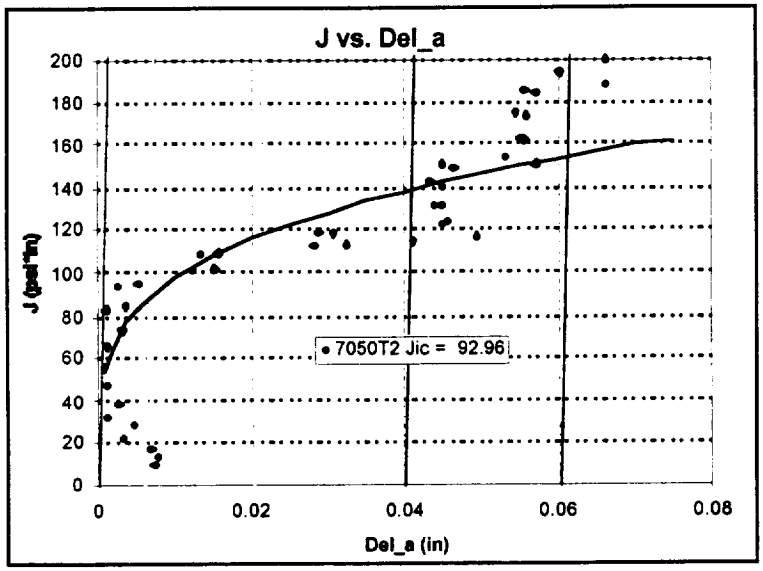

Figure 13 – *Fracture test results for specimen 7050T2*

Fracture Modeling

Fracture modeling consisted of studies on initiation and tearing processes. The bulk of the tearing work was performed at Ames, using cell-model meshes developed at Davis. These had cell sizes of 0.0005, 0.0015, and 0.016 inch for S17400, N07718, and S30400, respectively, and overall dimensions as stated in Table 4. Initiation modeling in A07050 was performed at Davis. These analyses employed focused meshes such as that shown Figure 14. Results of the tearing analyses are not currently available. Results of the initiation studies in A07050 are discussed in a later section of this report.

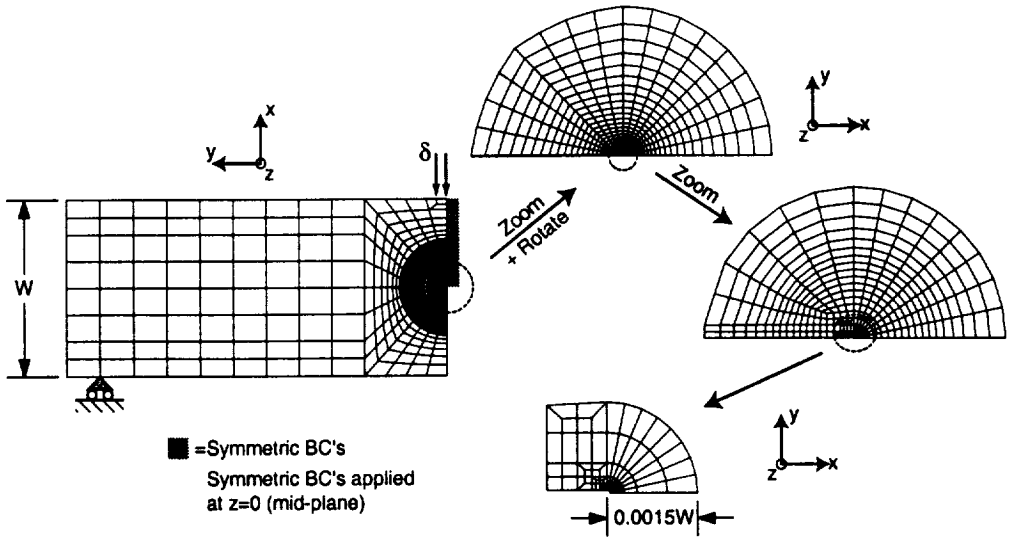

Figure 14 – *Typical mesh for analysis of fracture initiation.*

Residual Stress Measurements in A07050 Plate

Fracture testing of a small number of full thickness specimens taken from the A07050 plate caused non-uniform crack extension, and residual stress measurements were preformed to determine if they were the cause. The *J-R* curves reported above result from testing of half-thickness samples, where the samples were removed near the surface of the parent plate. Full-thickness samples were tested as part of a continuing program, but the resulting non-uniform growth raised concerns about the validity of the *J-R* curves presented above. An example of the crack growth pattern produced is shown below. Such profiles can be caused by either residual stresses or microstructure variation. To determine the effect of residual stresses on crack growth, opening mode residual stresses relative to the fracture specimen (transverse to the rolling direction of the plate) were measured through the plate thickness using the crack-compliance method. Measurements were made on a 1.0×0.5×6.0 inch rectangular specimen removed from the plate by conventional machining. The orientation of this blank had the 1.0 inch dimension running through thickness and the 6.0 inch dimension running transverse to the rolling direction. This specimen was cut along the 0.5 inch depth, incrementally through the 1.0 inch thickness. Strain released during cutting was used to back-compute residual stresses in the removed sample prior to cutting. Because the removed sample was of suitable size, the residual stresses measured were assumed to be identical to those in the parent plate prior to specimen removal. Residual stresses found in the plate were quite small, on the order of 3 ksi (maximum), as shown in the figure below. The conclusion reached was that microstructure and not residual stresses was the primary cause of the non-uniform crack growth. The microstructure variation is further discussed in a later section of this report.

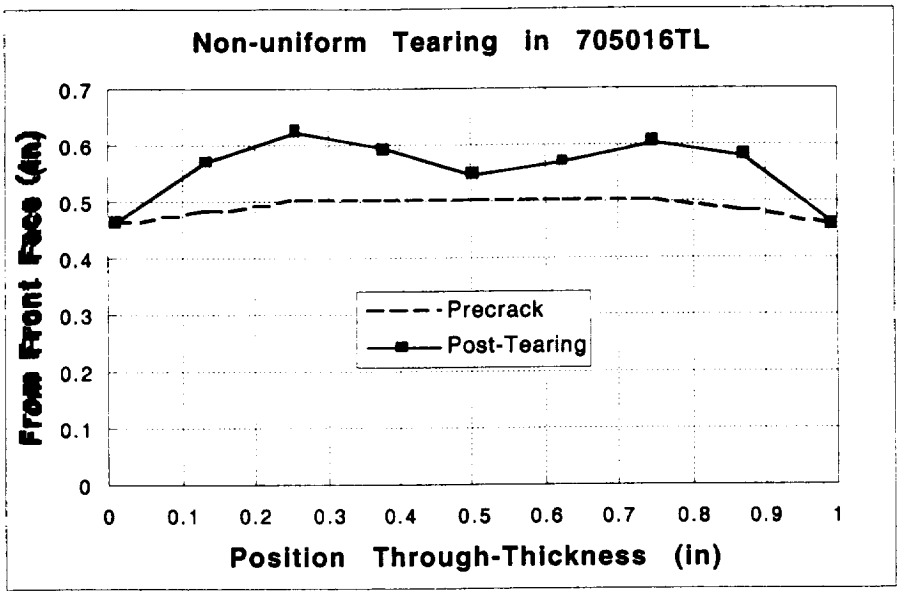

Figure 15 – *Non-uniform crack growth in 705016TL specimen (specimen was square, with W=B=1.0 inch)*

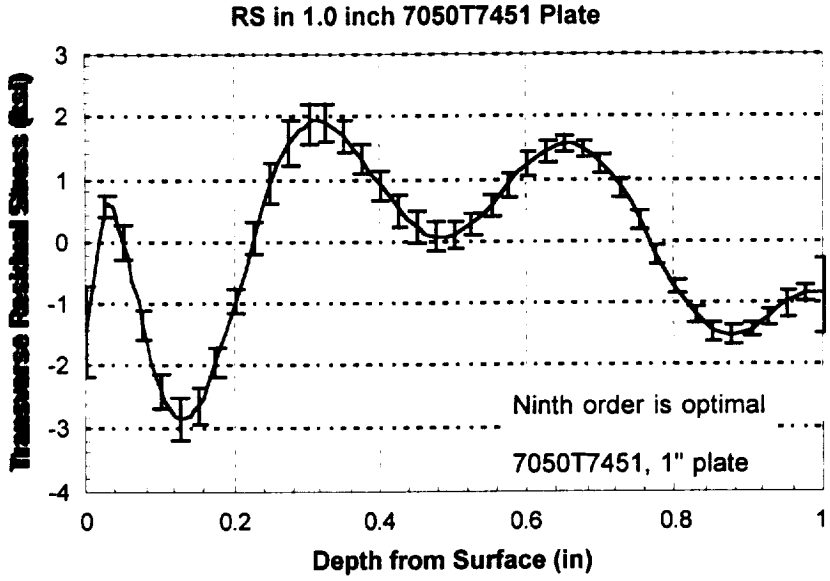

Figure 16 – *Residual stresses measured in 7050 T7451 aluminum plate*

Micromechanical Model Calibration for A07050

The following pages contain a recent submission to Engineering Fracture Mechanics regarding micromechanical modeling in A07050. The work described is the direct result of efforts on this project; therefore, the document is incorporated into this report. The paper demonstrates a number of issues regarding the calibration of micromechanical models for ductile fracture initiation, and will have bearing on the use of the data presented above in similar efforts in the future.

Micromechanical Modeling of Fracture Initiation in 7050 Aluminum

Michael R. Hill[1]

Mechanical and Aeronautical Engineering Department, University of California, Davis, CA, 95616, USA, mrhill@ucdavis.edu

Tina L. Panontin

Chief Engineer, NASA-Ames Research Center, Moffett Field, CA, 94035-1000, USA, tpanontin@mail.arc.nasa.gov

Abstract

Mechanical testing and finite element calculations have been carried out to characterize the fracture initiation behavior of the high-strength aluminum alloy 7050-T7451. Results show that fracture initiation is well-predicted for two specimen types of differing constraint using a stress-modified, critical plastic strain micromechanical model. The relation between stress triaxiality and critical plastic strain was found from a series of notched tensile specimens. Data from these tests were interpreted using both companion finite element modeling and common, semi-empirical relations, and these two approaches are compared. Multiple, interrupted tests of standard, highly constrained SE(B) specimens were used to obtain the *J-R* curve in 7050 for small amounts of tearing to experimentally identify initiation. Companion modeling and the stress-modified, critical plastic strain relation are then used to find the length scale for fracture, l^*, needed for initiation predictions. The *J*-integral corresponding to predicted fracture, J_c, is shown to monotonically increase with the value assumed for l^*. Calibration of the length scale is therefore achieved by locating the intersection of the computational J_c-l^* curve and the experimental *J-R* curve. The calibrated stress-modified, critical plastic strain relation and length scale are then used to predict fracture initiation of a low-constraint specimen. The prediction is within 5% of the experimental measurements. Finally, various aspects of the procedure followed in the present work are compared to previous efforts using similar approaches.

Key Words: fracture, aluminum, micromechanical modeling, constraint

1. Introduction

Fracture in high strength aluminum alloys generally occurs under small-scale yielding conditions. However, fracture may occur under various conditions of constraint, leading to a range of effective toughness in practical applications. Constraint is widely know to depend on geometry and loading type, and has recently been shown to be affected by residual and thermal loading [1][2][3]. Continuum micromechanical approaches, based on detailed modeling of the material response and a small number of empirical parameters, offer the promise of constraint-sensitive fracture prediction in a variety of materials. However, there have been relatively few descriptions presented in the literature of micromechanical fracture prediction in high strength aluminum alloys.

This paper describes the calibration and application of a model capable of predicting the onset of fracture in the high strength aluminum alloy 7050-T7451. The micromechanical

[1] Corresponding author. MAE Department, UC Davis, One Shields Avenue, Davis, CA 95616-5294, (530)754-6178, (530)752-4158 (FAX), mrhill@ucdavis.edu

model employed follows from the stress-modified, critical plastic strain model presented in [4], and provides a constraint-sensitive prediction. Mechanical testing is carried out on four tensile, uncracked geometries and two single edge notched bend bars with differing crack size. A systematic procedure is described for finding the length-scale needed for fracture prediction. Fracture predictions are presented and compared with the experimental data. The interpretations of tensile results using semi-empirical formulae or companion modeling are compared. Finally, methods used to experimentally determine tearing onset are contrasted relative to their applicability for calibration and verification of the model for fracture prediction discussed.

2. Material

The material investigated in this study is 7050-T7451, a high strength aluminum alloy. 7050 is an Al-Zn-Mg-Cu-Zr alloy developed to have a combination of high strength, high resistance to stress-corrosion cracking, and good fracture toughness. Compared with 7075, the use of zirconium in lieu of chromium reduces sensitivity to quenching, which results in high strength in thick sections. Plate in the T74-type temper has toughness levels equal to or higher than other conventional high-strength aluminum alloys. The 51 designation indicates mechanical stress relief by stretching. Nominal mechanical properties of this alloy are given in Table 1.

E, GPa (Mpsi)	*ν*	*S_u, MPa (ksi)*	*S_y, MPa (ksi)*	*elongation, %*	*K_{Ic} MPa $\sqrt{m}$ (ksi $\sqrt{in}$)*
71.7 (10.4)	0.33	520 (76)	470 (68)	11	27.5 (25)†

Table 1. Mechanical properties of 7050-T7451 plate (longitudinal orientation) [5].

† K_{Ic} from Alcoa Mill Products "Alloy 7050 Data Sheet", guaranteed minimum, TL orientation

Fracture in 7050, as in other high strength aluminium alloys, proceeds by nucleation and growth of voids which precipitate from second phase particles. That is, the mechanisms of fracture are ductile even though the level of toughness is usually low. Because of the low toughness, high strength aluminum alloys fail with limited plasticity, and in cracked structures plastic zone sizes are small enough that generally small-scale yielding conditions prevail at the crack-tip. Even so, constraint loss due to shallow cracks or tension loading will cause toughness elevation that would not be predicted by the application of single parameter fracture mechanics, whether elastic or elastic-plastic. Further, two-parameter approaches cannot be applied in a straight forward manner due to the dependence of ductile fracture mechanisms on both the stress and deformation states at the crack-tip. Therefore, a micromechanical approach that follows the evolution of the crack-tip stress and deformation state with increasing applied load, has been pursued in order to predict fracture.

3. Specimen geometries

Experimental testing and companion non-linear mechanical simulations of various specimen geometries were conducted in an effort to develop a micromechanical fracture assessment methodology in 7050. All physical specimens used in this study were removed

from a single 25 mm (1.0 inch) thick plate. The loading axis of all specimens was transverse to the rolling direction of the plate. Fracture specimens were oriented such that the crack was driven in the rolling direction (i.e, fracture specimens were TL). Six distinct specimen types were used in the study, four tensile and two fracture geometries as shown in Figure 1, with additional dimensions given in Table 2. Companion models of each physical specimen were constructed and analyzed using elastic-plastic finite element analysis. Where specimen diameter or thickness was less than that of the parent plate, specimens were removed as near to the plate surface as possible.

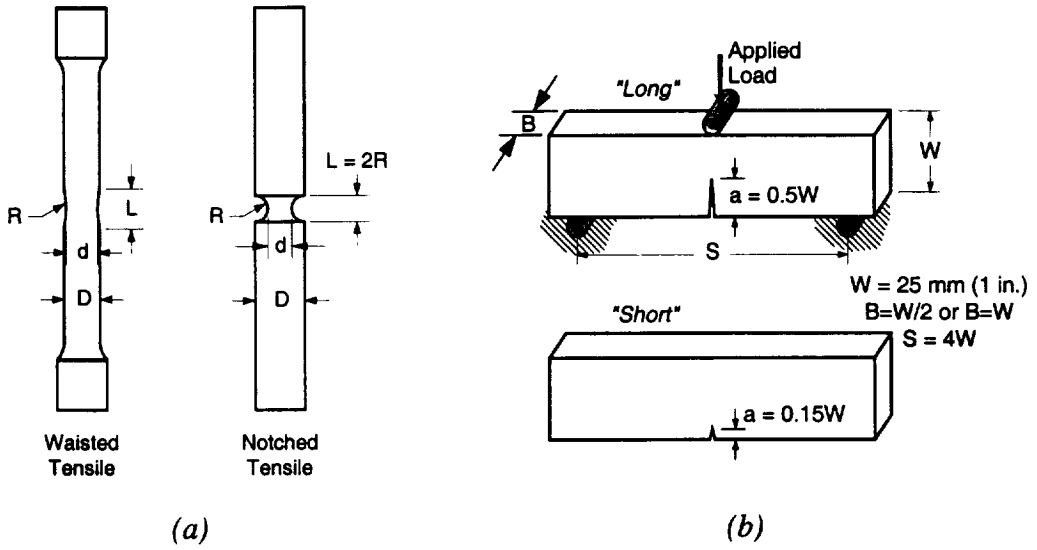

Figure 1. Specimens used in this study: (a) Tensile and (b) Long- and short-crack SE(B)

Designation	*D, mm (inch)*	*d, mm (inch)*	*R, mm (inch)*
Waisted	9.2 (0.362)	8.2 (0.322)	25.4 (1.0)
Large Notch	12.7 (0.5)	6.4 (0.25)	3.2 (0.125)
Medium Notch	12.7 (0.5)	6.4 (0.25)	1.6 (0.062)
Small Notch	12.7 (0.5)	6.4 (0.25)	1.0 (0.040)

Table 2. Tensile specimen dimensions (refer to Figure 1(a)).

Four separate tensile geometries were investigated, including waisted and notched specimens (Figure 1a). Waisted samples were used to determine tensile strength and flow properties. The waist in the specimen allows monitoring of diametral contraction during testing, so that true stress could be accurately monitored. Notched tensile specimens provided additional geometric constraint, relative to the waisted specimen, with sharper roots providing increased hydrostatic stress. Therefore, the tensile fracture behavior of this alloy was determined under differing conditions of geometric constraint.

Single edge notched bend (SE(B)) specimens were used to measure fracture properties in 7050 in the TL orientation. Two crack lengths were studied to elucidate constraint effects in sharp-crack fracture behavior of this material. So called long-crack ($a/W = 0.5$)

and short-crack ($a/W = 0.15$) specimens were tested. In the micromechanical framework, the long-crack specimens are used to provide calibration of a metallurgically relevant length scale. The short-crack specimens are then used to provide an independent qualification of the ability of the micromechanical approach to predict fracture under less constrained conditions.

4. Testing procedures

All specimens were tested at quasi-static loading rates in laboratory air under ambient temperature.

Tensile specimens were tested on a servo hydraulic testing system under computer control. Specimens were fixed in hydraulic grips carefully aligned to obtain pure tension loading. Axial extension and diametral contraction were monitored simultaneously using separate extensometers; axial extension was measured over a 50 mm (2 inch) gage length and a special diametral extensometer was fabricated with specimen contacts that would fit in the smallest notches used. All measured quantities (signals from the LVDT, load cell, axial extensometer, and diametral extensometer) were digitally acquired during the test at a rate of 4 Hz using a 16-bit digital data acquisition system. Loading rates resulted in quasistatic strain rates in all specimens up to fracture $10^{-5}/s \leq \dot{\varepsilon} \leq 10^{-1}/s$. Three replicate samples of each geometry were tested. Following testing, final failure-section diameter and elongation to failure were measured using a vernier caliper.

SE(B) specimens were tested in three-point bending following the procedures of ASTM E-1152 [6] using the same servo hydraulic testing system. Crack-mouth opening displacement (CMOD) was measured using a clip-gage with 6.4 mm (0.25 inch) initial gage length, and calibrated to measure 0.64 mm (0.025 inch) of opening. Tests were run in CMOD control. Measurements of CMOD, stroke, and load were gathered at 4 Hz. Loading rates were 2.5 μ/sec (0.0001 in/sec) and 0.51 μ/sec (0.00002 in/sec) for long- and short-crack specimens, respectively. Unloading compliance was used to monitor crack-extension, with unloading performed at steps in CMOD of 25 μ (0.001 inch) and 6.4 μ (0.00025 inch) for the long- and short-crack specimens, respectively. Unloading and reloading rates were similar to those previously mentioned, and data was gathered at 20 Hz during the compliance measurement.

Specimens were tested to various amounts of crack extension. An initial series of tests were run to the maximum amount of tearing allowed in E-1152 ($\Delta a_{max} = 0.05W$), producing single specimen crack growth resistance curves (R-curves). Following quasistatic three-point bend testing, each specimen was fatigued with maximum load equal to 75% of the load at which static testing was stopped, at a stress ratio of 0.33, to mark the region of stable tearing, and then fractured. The initial (precrack) and final (stable tearing) crack fronts were measured optically at nine locations, as stipulated in E-1152. Results revealed tunneled crack fronts in the non-side-grooved specimens, which induces error in crack length estimated by compliance [6]. Since the micromechanical calibration relies on accurate crack length measurement, a second series of tests implementing a multiple-specimen approach was used to determine the crack growth resistance curve near micromechanical fracture initiation. Specimens were tested, the amount of stable tearing marked by fatigue, then fractured. Crack fronts were then examined using both optical and scanning electron microscopes (SEM) to accurately determine the amount and location of maximum stable tearing.

5. Micromechanical model

Ductile fracture behavior is dependent upon both the stress and deformation state at the crack-tip. As mentioned above, the micro-mechanisms of ductile fracture in high strength aluminum alloys are void nucleation and growth, both of which initiate from second-phase particles within the microstructure [7]. In cracked geometries, plastic strain and hydrostatic stress at the crack-tip drive the nucleation and growth process. Mackenzie, et al., proposed a model which predicts the initiation of ductile fracture when equivalent plastic strain near the crack-tip, $\varepsilon'_p(r, \theta, z)$, exceeds a critical amount, $\varepsilon_p^{crit}(r, \theta, z)$ (where r, θ, and z are crack-tip centered cylindrical coordinates) [4]. In cracked bodies, this criterion must be met over some distance ahead of the crack-tip, l^*, representative of the distribution of microstructural features from which fracture progresses. The critical level of plastic strain is assumed to depend on the ratio of hydrostatic, $\bar{\sigma}(r, \theta, z)$, to von Mises stress, $\sigma'(r, \theta, z)$, at a given material point. The characteristic length, l^*, is related to the spacing of second-phase particles. The critical level of plastic strain can be written for many materials as [8]

$$\varepsilon_p^{crit}(r, \theta, z) = \alpha \exp\left(-\beta \frac{\bar{\sigma}(r, \theta, z)}{\sigma'(r, \theta, z)}\right) \tag{1}$$

Here, α and β are empirical constants, fitted to data obtained from tests and analyses of notched tensile specimens [4]. To predict fracture initiation, one can compute the parameter

$$\mathrm{SMCS}(r, \theta, z) = \varepsilon'_p(r, \theta, z) - \varepsilon_p^{crit}(r, \theta, z) \tag{2}$$

where SMCS reflects the common name for this general approach: stress modified, critical (plastic) strain [9]. For a given loading condition, fracture is predicted when

$$\mathrm{SMCS}(r, \theta, z) \geq 0 \text{ for all points } r \leq l^*,\ \theta = \bar{\theta},\ z = \bar{z} \tag{3}$$

In this expression it is recognized that ductile fracture will not necessarily initiate directly ahead of the crack-tip (i.e., at $\theta = 0$), but possibly at an oblique angle $\theta = \bar{\theta}$ and arbitrary position along the crack front, $z = \bar{z}$. In application, $\bar{\theta}$ and $\bar{z}$ are found by monitoring the SMCS parameter with increasing load and noting the location where Equation (2) is first satisfied.

6. Analysis procedures

6.1 Finite Element Analyses

Computational mechanics are carried out using a commercial non-linear finite element code [11]. Large-strain formulation is used in the continuum mechanics. The material model assumed is homogeneous and elastic-plastic, using incremental, isotropic, J_2 plasticity. For fracture specimens, the J-integral is computed using the domain integral approach. To obtain a better match with experimental estimates of the J-integral, all values given for J are weight averaged by volume, though the specimen thickness, along the crack-front [12]. Small load steps are taken during the analysis to ensure that the historical development of plastic deformation is accurately captured.

Typical finite element meshes used in this study are shown in Figures 3 and 4. Care was taken to obtain mesh refinement capable of resolving strain gradients in the failure regions. The tensile meshes shown in Figure 3 reflect the symmetry of the specimen configuration and the axisymmetric model used in the analysis. The SE(B) meshes shown in

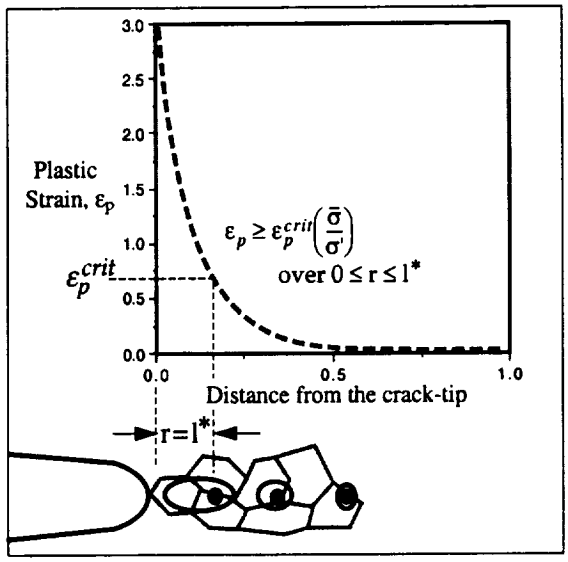

Figure 2. Schematic representation of the micromechanical fracture initiation model (after [*10*]).

Figure 4 reflect the two planes of symmetry in these specimens, one about the load line and one about the specimen mid-thickness. The SE(B) mesh layout through-thickness (in the *z*-direction) has ten layers of elements, with a geometric progression of layer thickness such that the free surface elements are ten times thinner than those at the mid-thickness. The SE(B) mesh has a small initial radius at the crack-tip in anticipation of crack-tip blunting. This radius is r_o = 1.27 μ (50 μinch), small enough to have a negligible effect on strains at micromechanically relevant distances from the crack tip. The effect of the radius on crack-tip strain fields was investigated by constructing developmental meshes with crack-tip radii of 0.254, 1.27, and 5.08 μ (10, 50, and 200 μinch); negligible differences were found between models with the two smallest radii at relevant distances from the crack tip. Several elements were placed just behind the crack-tip for accurate monitoring of the crack-tip opening displacement, defined as the crack-face opening at an angle of 45° from the crack-tip in the deformed configuration. Computationally determined crack-tip opening displacement (CTOD) at experimentally determined fracture initiation indicate that r_o < CTOD/10, a mesh design guideline suggested by Anderson [*13*].

6.2 Data Reduction Procedures

Data from companion models of the waisted samples were used with gathered experimental data to determine the flow curve for 7050-T7451. For the non-linear analyses pursued here, a true stress versus logarithmic strain curve is required, and neither quantity is directly measured during a tensile test. A first estimation of the flow curve was provided directly from reduction of the experimental data by using measured waist diameter to compute true stress and log strain using

$$\sigma_i = 4P_i/(\pi d_i^2) \tag{4}$$

and,

$$\varepsilon_i = 2\ln(d_o/d_i) \tag{5}$$

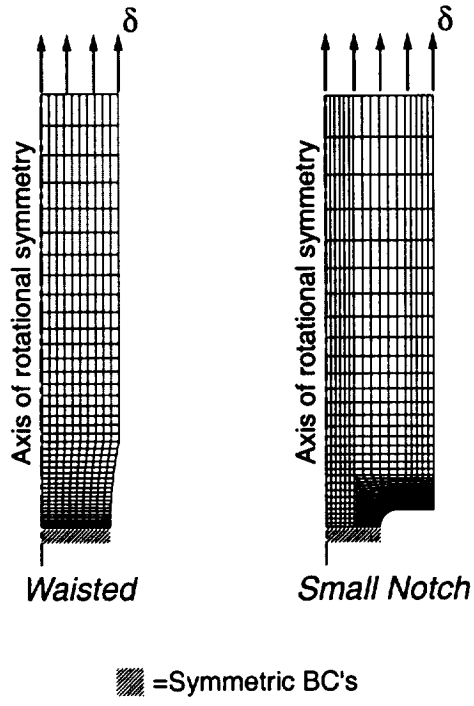

Figure 3. Finite element meshes of waisted and small notch tensile specimens.

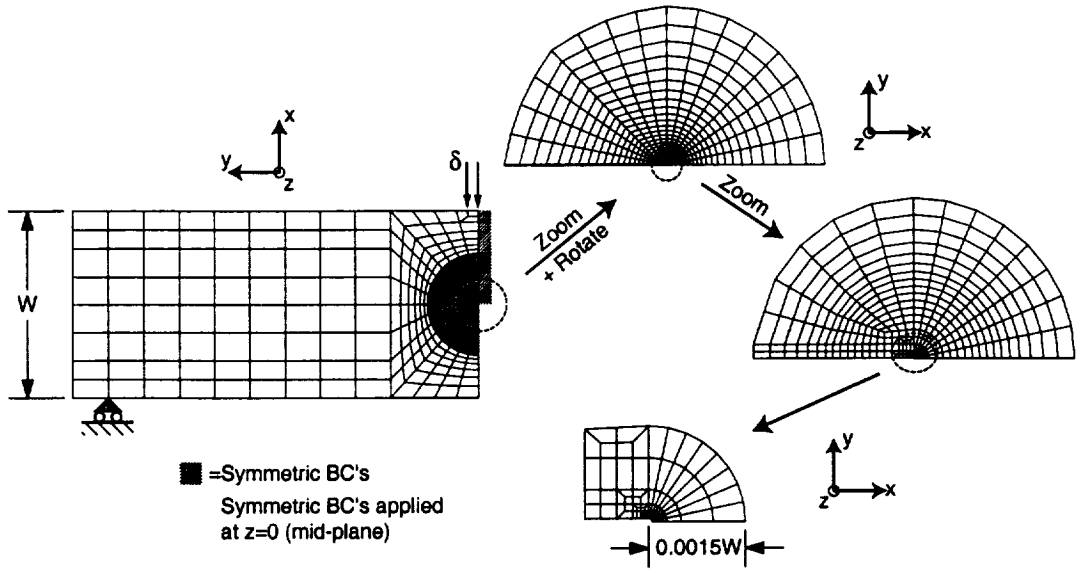

Figure 4. Finite element mesh of the long-crack SE(B) ($a/W = 0.5$).

where P is the applied load, d is diameter, and where the subscripts o and i refer to the initial and current states. This flow curve is inaccurate because it ignores the triaxiality of the stress state in the specimen neck and provides only an approximation to the logarithmic strain [*14*]. An improved approximation to the actual flow curve was obtained by performing an elastic-plastic simulation of the waisted tensile test, and iterating on the

flow curve used until a match was obtained between computed and measured trajectories of engineering stress versus diametral strain. The flow curve determined in this way was used in all further analyses.

Companion models of all tensile specimens were used to provide data for the SMCS correlation between stress triaxiality and equivalent plastic strain at fracture. The work by Mackenzie, et al [4] used semi-empirical relations to determine triaxiality and plastic strain in tensile specimens at failure:

$$\frac{\bar{\sigma}}{\sigma'} = \frac{1}{3} + \ln\left(\frac{d_o}{4R_o} + 1\right) \tag{6}$$

$$\varepsilon_p = 2\ln(d_o/d_f) \tag{7}$$

Where d is diameter, R is notch root radius, and where the subscripts o and f refer to the initial and failure states. Results of these calculations were used to correlate critical plastic strain to triaxiality. Panontin and Sheppard [15] made use of finite element analysis to determine more accurate distributions of the stress and strain state in the tensile specimens employed in their study. This later approach was pursued here, and its advantages are demonstrated below. The companion models of each tensile specimen are analyzed to the point of final fracture observed in the laboratory. Comparison between experiment and companion model is made based on the trajectory of diametral strain and engineering stress. Because these trajectories do not match exactly, the failure point in the companion model is assumed to be where the computed diametral strain is equal to the measured diametral strain at fracture, averaged over the three replicate specimens. At this point in the simulation, stress triaxiality and equivalent plastic strain at the center of the specimen neck are used as a data point on the critical plastic strain failure curve of the SMCS model.

Data from the companion model of the long crack SE(B) specimens are used to calibrate the length scale in the SMCS criterion. The particular value set for the length scale in the SMCS model will greatly influence the performance of the criterion. In concept, the value used should be set based on microstructural and fractographic information. In practice, the variability of the fracture process, even as exhibited on a single fracture surface, prevents the exclusive use of experimental observation to set the length scale. In the current effort, computational results are used together with fractographic evidence to obtain the length scale used in the model. Fractography is used to estimate an acceptable range for the length scale. Analysis is used to find a value of the length scale within this range to match experimental fracture observations.

Calibration of the length scale is achieved by predicting fracture, using the SMCS criterion with a range of length scales, and comparing these results to experimental evidence. Parameters α and β in the relation for $\varepsilon_p^{crit}(r, \theta, z)$, Equation (1), are determined from tensile specimens, and held fixed. Then, for a set of values of the length scale, historical crack-tip stress and strain results from the simulation are used to find the point in the analysis where SMCS first becomes positive over the given length scale. As will be shown, the J-integral at satisfaction of the SMCS criterion (Equation (3)) monotonically increases with the length scale. Comparison with experiment follows two key assumptions. First, it is assumed that satisfaction of the SMCS criterion results in crack extension equal to the length scale [16]. Second, it is assumed that the J-integral computed from experimental data (using ASTM E-1152 [6]) and from the simulation (using the volume averaged domain integral results) were comparable [17]. Using these two concepts, the calibrated

length scale is found by locating the intersection of the experimental R-curve (J-Δa data) with the computational trajectory of J-integral at satisfaction of the SMCS criterion for the range of assumed length scales. As will be shown, this procedure resulted in a length scale within the range of fractographic and microstructural evidence.

Data from the companion model of the short crack SE(B) specimens are used to assess the accuracy of the SMCS approach.The long-crack SE(B) specimens used in calibration of the SMCS criterion represent a well-constrained geometry. The short-crack specimens exhibit a higher toughness and provide a point of qualification for the SMCS approach. If the SMCS approach can accurately predict the initiation of tearing in both SE(B) specimen types, then we will conclude that the model is capable of predicting fracture in cracked bodies, at least over the range of constraint represented by the long- and short-crack specimens.

6.3 CONSTRAINT ANALYSES

The change in constraint conditions at the crack tip in the SE(B) specimens due to the influence of crack length is quantified using J-Q theory. The theory uses the approximate two-parameter description of the crack-tip stress-strain fields developed from asymptotic analyses and finite element simulations performed by O'Dowd and Shih [*18*][*19*]. These stress fields are applicable to small and large scale yielding conditions and can be written as

$$\sigma_{ij} = \sigma_o \cdot f_{ij}\left(\frac{r\sigma_o}{J}, \theta, Q\right) \tag{8}$$

where r and θ are polar coordinates centered at the crack-tip and the parameter Q is dimensionless. As a measure of how much σ_{ij} differs from the adopted small scale yielding (SSY), $T = 0$ reference solution at the same applied J, the parameter Q has been shown to characterize the magnitude of the hydrostatic stress over the forward sector ahead of the crack-tip (i.e., $|\theta| < \pi/2$ and $1 < r/(J/\sigma_o) < 5$) to a good approximation. Q is formally defined as

$$Q = \left(\frac{\sigma_{\theta\theta} - \sigma_{\theta\theta}\big|_{SSY;T=0}}{\sigma_o}\right) \text{ at } \theta = 0, \left(\frac{r\sigma_o}{J}\right) = 2 \text{ to } 5 \tag{9}$$

and is obtained from stresses predicted straight ahead of the crack-tip by finite element analyses of both finite and infinite size (SSY) crack geometries. By definition, $Q = 0$ in all crack geometries under tensile mode one loading and in small scale yielding conditions. However, as deformation levels increase in finite size specimens, the hydrostatic stresses at the crack-tip are relieved and fall below those that exist in an infinite cracked body at the same J-value. This produces a negative Q-value, which denotes a loss in constraint. A positive Q-value indicates that high constraint exists for a particular geometry and loading condition [*20*].

We rely on the J-Q analyses to indicate the range of constraint over which the fracture prediction scheme adopted has been qualified. It is possible to use a variety of parameters to quantify constraint, including Q, the T-stress, and triaxiality (the ratio of hydrostatic stress to vonMises equivalent stress, $\bar{\sigma}/\sigma'$). The T-stress is meritorious because it can be computed from an elastic analysis. As such, it *infers* the state of stress and strain at the crack-tip in small-scale yielding, but does not *describe* the crack-tip state

as well as does Q. The triaxiality ratio provides quantitative information at the crack-tip, but is a local parameter and hence has a spatial dependence. Because Q quantitatively describes the crack-tip stress state over a microstructurally relevant region near the crack-tip, it was selected as a basis for specifying the range of constraint over which the SMCS criterion has been verified for use in 7050-T7451.

7. Results

7.1 Tensile Properties

Waisted specimens were used to determine strength properties of the 7050-T7451 plate in the transverse direction. Handbook values for elastic properties, shown in Table 1, were assumed to be valid. Axial engineering stress-strain data gave 0.2% offset yield strength of σ_o = 531 MPa (77.0 ksi) and ultimate strength of S_u = 578 MPa (83.9 ksi).

7.2 Flow Properties

Results of tensile testing and companion modelling of waisted samples also provided data to obtain the flow curve for 7050-T7451. A plot of engineering stress versus diametral strain from a single waisted sample is shown in Figure 5. These data were reduced to find an initial flow curve, using Equations (4) and (5), as shown in Figure 6. The finite element load and displacements results, obtained using this initial flow curve, were reduced and are plotted with the experimental engineering stress and strain in Figure 5 (labeled as "Simulation (initial)"). The initial flow curve does not provide the correct response due to hydrostatic stress present in the initially waisted specimen. The initial flow curve was altered through iteration to obtain a match between the measured and calculated engineering stress versus diametral strain trajectories. The resulting deformation history is plotted in Figure 5 (labeled as "Simulation (final)"). The flow curve resulting from iteration is shown together with the initial flow curve in Figure 6. The Bridgman correction [*21*] might be applied to estimate the effective hardening of the material due to triaxial stress in the necked specimen. Results of using a particular correction scheme [*14*] based on Bridgman's work are shown in Figure 6, and do not agree with the amount of artificial hardening caused by triaxial stresses indicated by the simulation. This discrepancy is due both to the approximate nature of the Bridgman correction and to the presence of the *initial* neck in the specimen which is not accounted for. The flow curve obtained though iteration and shown in Figure 6 is used in all further analyses.

Simulation using the flow curve obtained from the waisted samples does not result in an entirely accurate prediction of the behavior of the notched tensile samples. Examples of the measured and predicted engineering stress and diametral strain in notched geometries are shown in Figure 7. It is clear from these data that decreasing notch radius (i.e., increasing triaxiality) results in over-prediction of the engineering stress. In fact, the engineering stress is over-predicted by 9.4% at failure of the small-notch specimen, while simulation using the same flow curve results in negligible error for the waisted specimen (see Figure 5). Experimental data from only a single test are shown in Figures 5 and 7, but variability from specimen to specimen is negligible. Further, finite element meshes were refined until there was no further change in material response with an increased number of elements. Therefore, it appears that isotropic, J_2 plasticity may not faithfully represent the actual material response with increasing triaxiality. Since the purpose of the companion

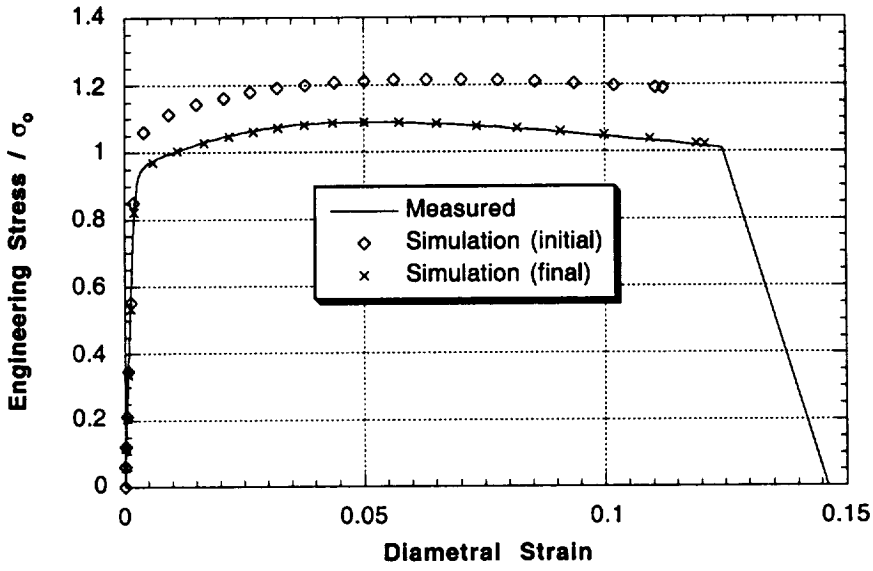

Figure 5. Engineering stress versus diametral strain in a waisted tensile sample.

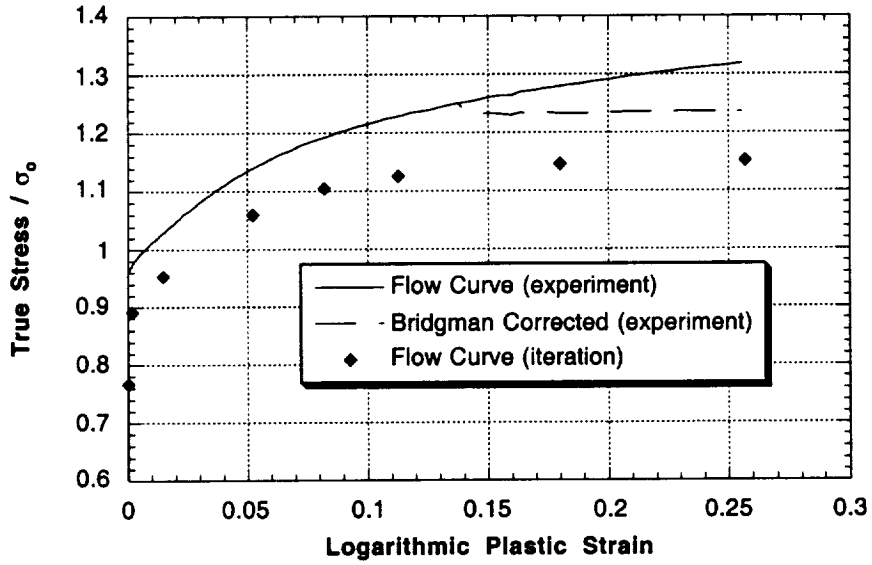

Figure 6. Estimated and corrected flow curves for 7050 found from waisted samples.

models is to determine a failure rule such errors are of concern. However, failure in the computation is defined from deformation, by matching diametral deformation with the experiment. Therefore, the error in engineering stress shown in Figure 7 will not necessarily equate to similar error in the correlation of triaxiality and plastic strain at failure.

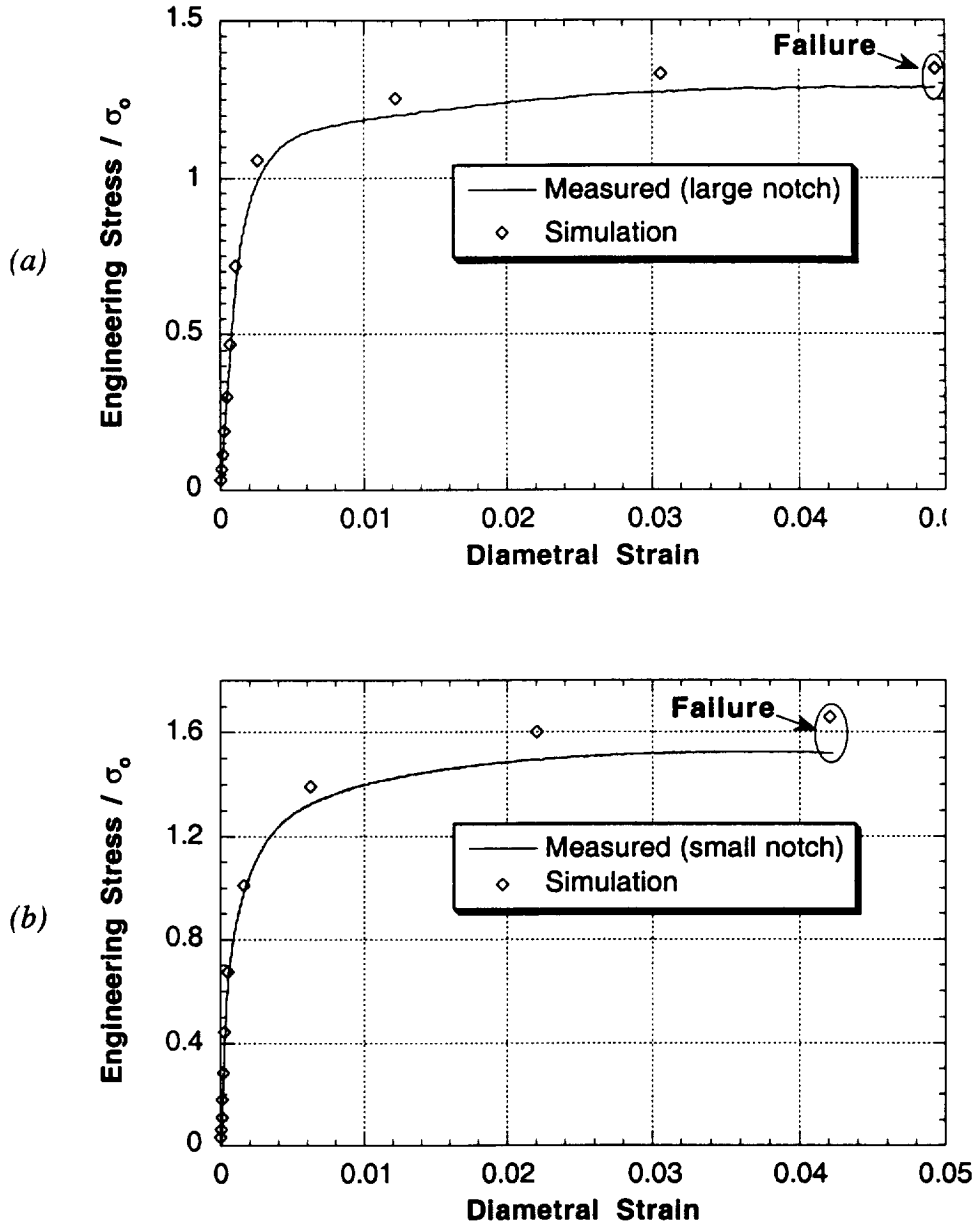

Figure 7. Engineering stress versus diametral strain in (a) large- and (b) small-notched tensile samples.

7.3 Critical Plastic Strain Correlation

Triaxiality and equivalent plastic strain at failure from the tensile specimens define the SMCS failure prediction curve for 7050-T7451. For a given geometry, when the finite element simulation reaches the level of diametral strain where failure occurred in the experiment, the distribution of stress and strain are examined. The simulation data reveal that there is a variation of stress and strain across the specimen neck, and that this variation is small at the center of the specimen. For example, the distribution of equivalent plas-

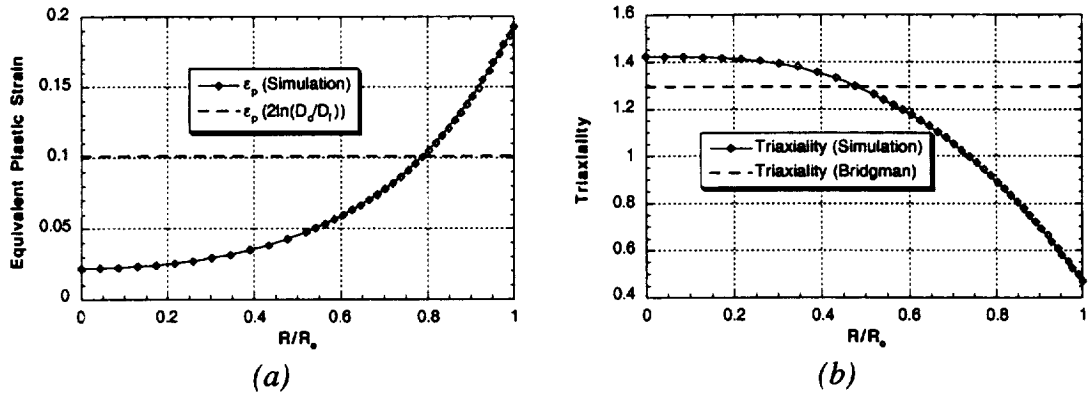

Figure 8. (a) Equivalent plastic strain and (b) triaxiality versus radial position in the neck of the small-notch specimen at failure conditions.

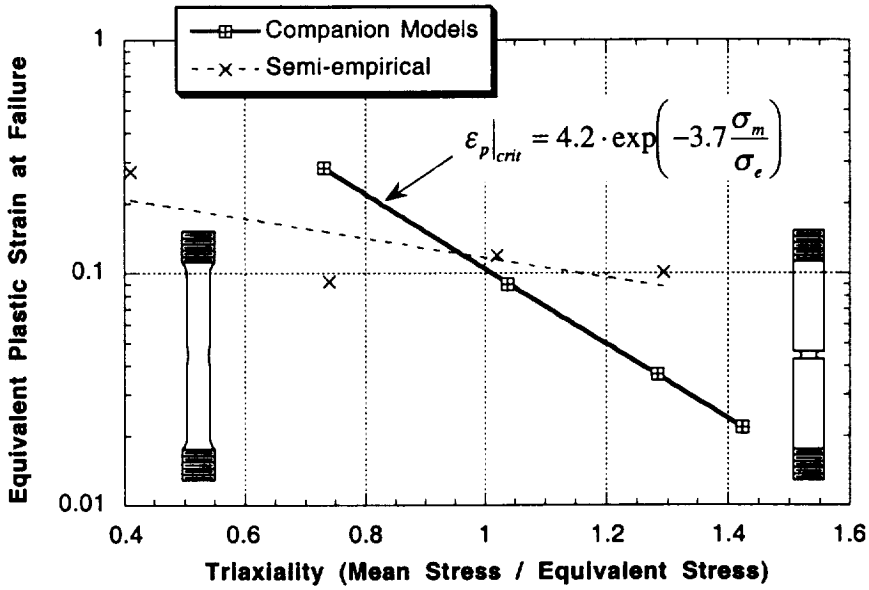

Figure 9. Equivalent plastic strain at failure versus triaxiality for all tensile geometries.

tic strain and triaxiality for the small-notched specimen are shown in Figure 8. It can be seen that a uniform state of stress and triaxiality occurs over about 15% of the specimen neck. Since this region is very large compared to microstructural features causing fracture, the values of plastic strain and triaxiality at $r = 0$ are used for further analysis. Also shown in Figure 8 is the triaxiality and plastic strain computed from Equations 6 and 7. This data clearly establishes the need for the companion models employed, as the semi-empirical relations provide a poor estimate of the conditions at the center of the neck, where failure initiates.

Combining results for all tensile geometries results in the dependence of critical plastic strain on triaxiality shown in Figure 9. Again comparing the companion modeling

and semi-empirical approaches, it is clear that the modeling approach provides the clearer correlation between plastic strain and triaxiality. The semi-empirical approach consistently underestimates triaxiality. For smooth samples, the semi-empirical approach provides a reasonable estimate of plastic strain, but over-estimates plastic strain in notched samples. Further, we see that Equation (1) provides an excellent correlation to the data from companion models over the range of triaxiality exhibited in the tensile specimens. The critical plastic strain parameters for 7050-T7451 are therefore $\alpha = 4.2$ and $\beta = 3.7$.

7.4 Length Scale Calibration with Multiple Specimen Data

The length scale in the SMCS criterion is determined by using experimental, multiple specimen *R*-curve data with the foregoing correlation between triaxiality and plastic strain and SE(B) simulation results for crack-tip stress and strain. The multiple specimen *R*-curve for long-crack SE(B) specimens at small levels of crack extension is shown in Figure 11. The four test results are from specimens with a range of initial crack-size ($0.47 \le a/W \le 0.53$), very close to the size used in the SE(B) companion model ($a/W = 0.5$). Maximum values of crack extension are plotted on the *x*-axis. Maximum crack extension occurred at approximately one-quarter of the thickness from the specimen surface (i.e., off the specimen midplane), always toward the free-surface of the parent plate. Since specimens were half-thickness of the parent plate, this suggests that the intrinsic material toughness is lower near the plate surface and depends on through-thickness location. Subsequent metallography revealed a through-thickness microstructure variation in the parent plate. Grains were small and equiaxed near the surface and were large and elongated near the plate center. In addition, there was a significant increase in the volume fraction of grain-boundary precipitates near the plate surface. Both of these factors have been shown to decrease fracture resistance in overaged Al-Zn-Mg alloys [7].

Simulation crack-tip stress and strain data are used to derive SMCS results for crack-initiation, and these are plotted with the experimental results in Figure 11. Each data point in the SMCS trend corresponds with a pair of *J*-integral and length scale. For a particular choice of length scale, the *J*-integral where the SMCS criterion is first satisfied is determined from the historical crack-tip stress and strain data. First, all nodal locations ahead of the crack-tip with radial position equal to the length scale are identified (note that the mesh has concentric rings of elements near the crack-tip, over $0 \le \theta \le \pi/2$ (see Figure 4)). Next, we compute SMCS, from Equations 1 and 2, at each node with $r = l^*$ from nodally averaged stress and strain results. At some time in the analysis, SMCS will be positive at $r = l^*$. Since the plastic strain distribution at the crack-tip is monotonically and sharply decreasing, as shown in Figure 2, SMCS will also be positive for $r < l^*$, indicating satisfaction of Equation (3) between the current and the previous time steps. Linear interpolation is then performed on the SMCS parameter to find the global loading parameters (load and *J*-integral) at fracture initiation (i.e., when SMCS = 0). The node at which SMCS first becomes positive also identifies $\bar{\theta}$ and $\bar{z}$ in Equation (3).

The *J*-integral thus obtained is plotted versus a number of assumed length scales in Figure 11. We define the calibrated length scale where the SMCS locus intersects the trend in the experimental results. Therefore, the above procedure results in a calibrated length scale for 7050-T7451 of $l^* = 0.006W$, or 0.15 mm (0.0060 inch). The failure criterion is first satisfied for $\bar{\theta} = \pi/4$ and $\bar{z} = 0$ (i.e., specimen mid-plane), independent of the length scale assumed.

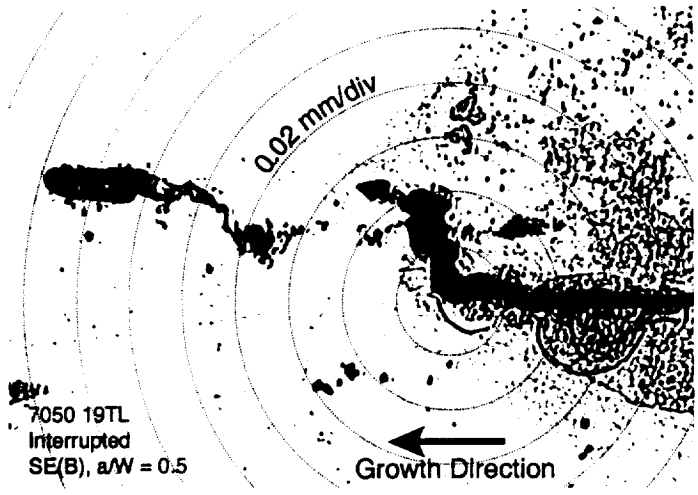

Figure 10. SE(B) specimen sectioned following fracture testing to $J/(B\sigma_o) = 1.83 \cdot 10^{-3}$

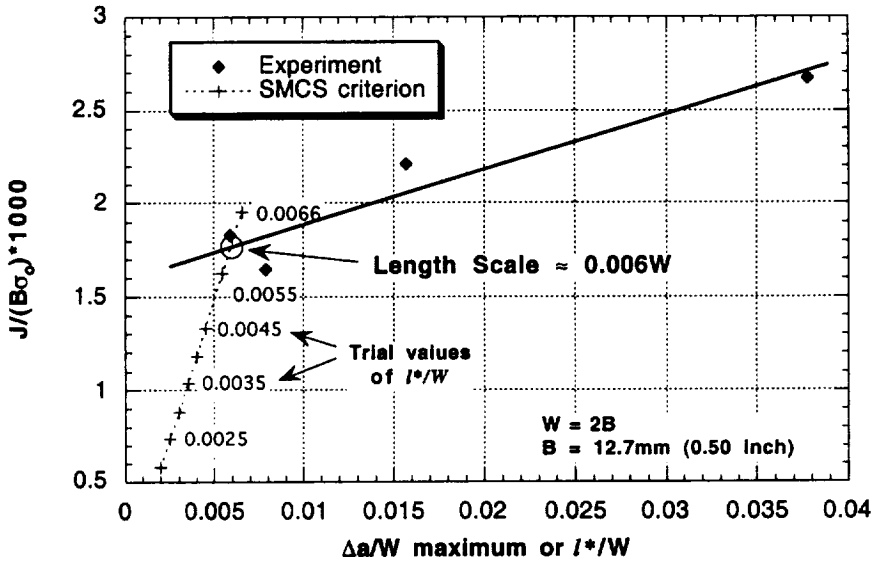

Figure 11. Long-crack specimens: *J*-integral versus crack extension from experiment and *J*-integral versus length scale from simulation; the two curves converge at $l^* = 0.006W$

7.5 Application to Low-Constraint Geometry

Comparison of experimental and computational results for the short-crack SE(B) provides a measure of accuracy of the SMCS approach. Experimental crack extension results and simulation predictions for short-crack specimens are shown in Figure 12. The three experimental results are from specimens with a small range of initial crack-size, $0.15 \leq a/W \leq 0.16$, close to the size used in the short-crack companion model ($a/W = 0.15$). Comparing the experimental results in Figures 11 and 12, we note the short crack specimens exhibit higher toughness. The toughness at 0.152 mm (0.0060 inch) of crack

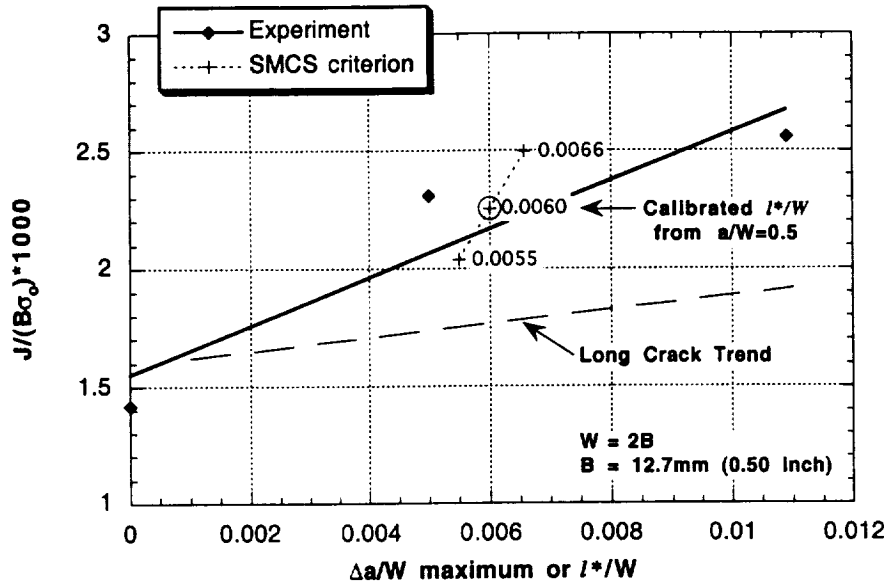

Figure 12. Short-crack specimens: J-integral versus crack extension from experiment and J-integral versus length scale from simulation. The calibrated length scale, 0.006 W, provides an accurate prediction.

growth is $J/(B\sigma_o) = 1.77 \cdot 10^{-3}$ in the long-cracked body and increases by 22% to $2.16 \cdot 10^{-3}$ in the short-cracked body, based on the trendlines. Crack extension is maximized along the crack front away from the midplane, as occurred in the long-crack specimens, presumably due to variation in intrinsic toughness along the through-thickness direction. The micromechanical approach, using the length scale calibrated from the long crack geometry, provides an accurate estimate of the toughness increase. The SMCS criterion is first satisfied for $\bar{\theta} = \pi/4$ and $\bar{z} = 0$ and results in a toughness of $J/(B\sigma_o) = 2.27 \cdot 10^{-3}$ for the short-crack geometry, having an error of 5% with respect to the trend.

The short-crack SE(B) geometry exhibits lower crack-tip constraint than the long-crack geometry and therefore higher toughness. Simulation results comparing crack-tip conditions on the midplane ($z = 0$) at the same level of J-integral in the two SE(B) geometries are shown in Figure 13. The particular value of J-integral where the two geometries are compared is just prior to failure of the long-crack geometry. Figure 13(a) shows that plastic strain at the crack-tip is similar, with both bodies having considerably more plastic strain on $\theta = \pi/4$ than on $\theta = 0$. The stress-state at the crack-tip is considerably different, with lower triaxiality for the short-crack geometry. At this level of deformation, then, each crack-tip has a similar level of plastic strain and the long-crack has higher triaxiality, which together indicate that the long-crack specimen is closer to failure.

The tendency toward failure is evident when the SMCS parameter, given by Equation (2), is plotted versus radial position on the specimen midplane ($z = 0$), as shown in Figure 14. In the SMCS model, failure occurs when material within one length scale of the crack-tip exceeds the triaxiality-dependent level of plastic strain shown in Figure 9. The SMCS parameter is positive when a point exceeds this strain, and negative when it does not. Larger values on the ordinate of Figure 14, then, indicate points that are

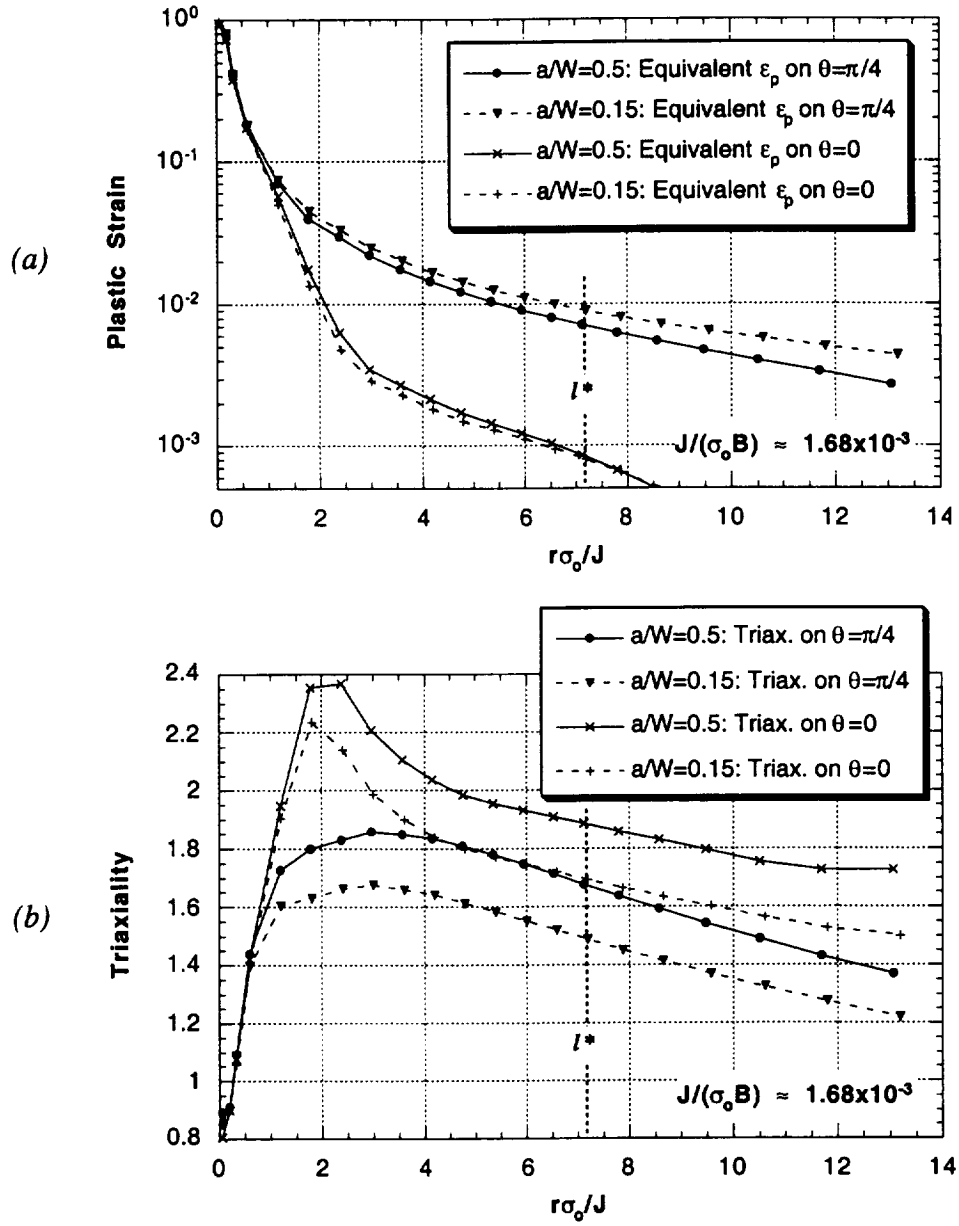

Figure 13. Comparison of crack-tip stress and strain state in long- and short-crack.SE(B) models: (a) equivalent plastic strain, and (b) triaxiality. All data from the specimen mid-plane ($z = 0$).

further along toward failure, but failure is not indicated until a point, one length scale from the crack-tip, has SMCS > 0. For reference, the calibrated length scale ($l^* = 0.006W$) is indicated in Figures 13 and 14. At this radial distance, the point on $\theta = \pi/4$ in the long-crack specimen is the furthest along in the failure process. In fact, as the load increases to failure, this point is where SMCS first becomes positive. Figure 14 further shows that close to the crack-tip, the SMCS parameter is larger on $\theta = \pi/4$ for both geometries, and that on either orientation, the long-crack specimen is closer to failure.

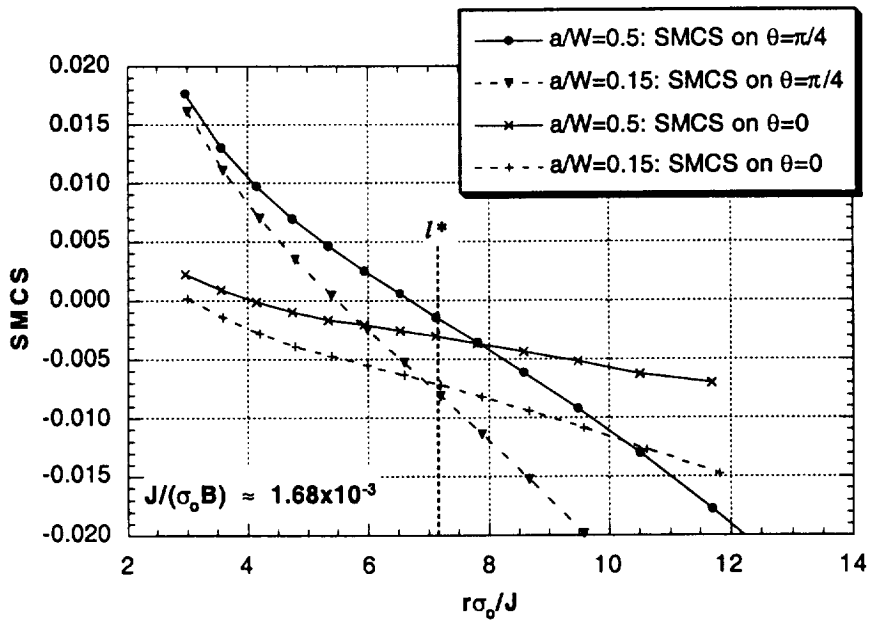

Figure 14. Effect of differing crack-tip stress conditions on the SMCS micromechanical parameter.

7.6 Constraint Range Examined

Using *J-Q* analysis, we can explore the range of constraint over which the accuracy of the SMCS micromechanical fracture prediction scheme has been examined. *J-Q* trajectories for the long- and short-crack specimens are shown in Figure 15. These are in general agreement with results presented in [*20*]. The data in Figure 15 indicate that the SMCS criterion is sensitive to constraint loss, predicting a 28% increase in toughness for a -0.22 change in Q. Given the results above, SMCS provides good accuracy over this range. If qualification of the criterion were desired over a wider range of constraint, a center-cracked tension panel could be used to produce fracture in conditions with $Q \approx -0.5$ [*20*].

7.7 Single Specimen R-curves

Tests of long- and short-crack specimens to large amounts of tearing were also performed. Single specimen *R*-curves, measured using unloading compliance, are shown in Figure 16. Obtaining an initiation toughness measure from these data is problematic using the data reduction scheme for J_{Ic} in ASTM E-813 [*22*]. The assumed relationship between J and Δa in E-813 (a power curve in Δa), together with data-exclusion at small amounts of tearing, results in a trendline that does not represent the data, as shown in Figure 16. An alternate scheme was used here to determine a toughness measure from these data, using a linear fit for data in the range $0.001 \le \Delta a/W \le 0.025$. As shown in Figure 16, the linear fit gives a more reasonable representation of the data at small amounts of crack extension ($\Delta a/W \le 0.02$) than does the power fit of E-813. A single value of toughness was determined by evaluating the linear fit at $\Delta a/W = 0.006$. Results for each specimen and data fit are shown in the table inset of Figure 16. The average toughness determined from the linear fit is $J/(B\sigma_o) = 2.34 \cdot 10^{-3}$.

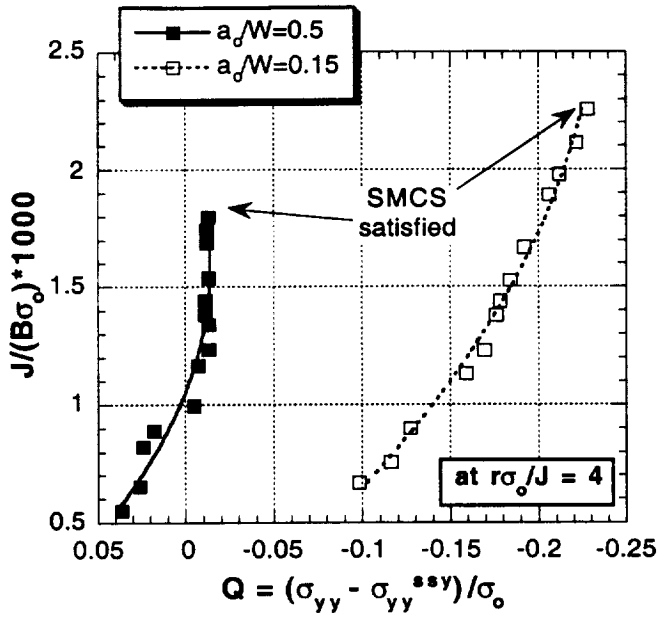

Figure 15. J-Q trajectories for the long- and short-crack SE(B) specimens.

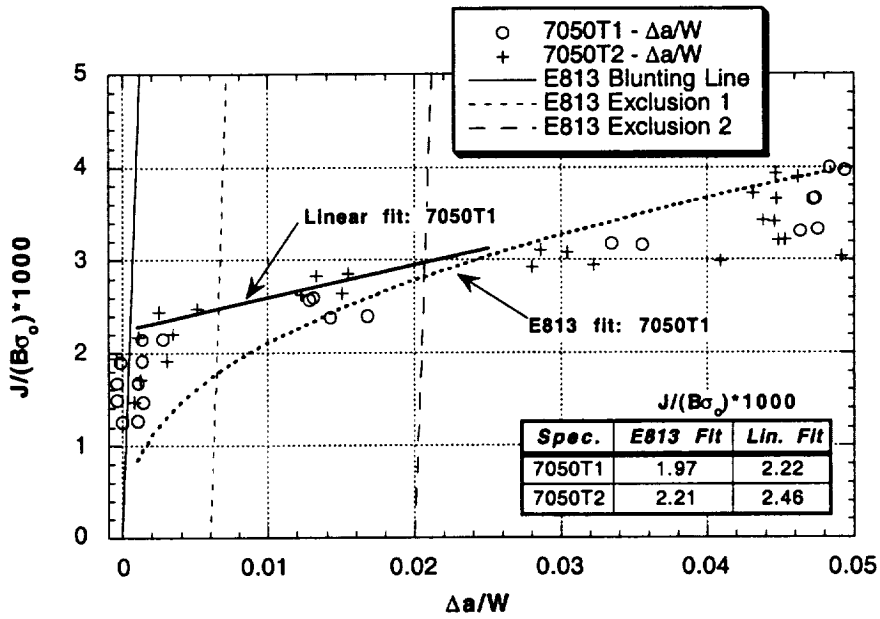

Figure 16. Long-crack specimens: *J*-integral versus crack extension, as measured using unloading compliance, with power (E-813) and linear fits to the data.

For short-crack specimens, it is well-known that unloading compliance cannot provide a reliable measure of crack extension. Instead, data reduction for K_{Ic}, according to ASTM E-399 [*23*], was used to determine a toughness measure for three short-crack specimens. In these analyses, the toughness depends on the initial crack length in the speci-

men, which is measured with microscopy following the test. The E-399 data reduction was also used for the long-crack specimens to provide comparative data. For for comparison with the previous results, K_Q was found using relations in E-399 and converted to J_{KQ} using

$$J_{KQ} = (K_Q^2/E)(1-\nu^2). \tag{10}$$

Toughness of the three short crack specimens was found to be $J_{KQ}/(B\sigma_o) = 2.58\cdot10^{-3}$, $2.61\cdot10^{-3}$, and $2.76\cdot10^{-3}$. Toughness of the two long crack specimens was found to be $J_{KQ}/(B\sigma_o) = 2.11\cdot10^{-3}$ and $2.22\cdot10^{-3}$.

8. Discussion

The results of the work above reflect a number of choices made in the analysis and reduction of experimental data and results from companion models. The following paragraphs provide some comparative assessment of the choices made in formulating the above approach. Three major choices were made in the above which differ from other published studies: 1) companion models were used to interpret the results of tensile testing; 2) the SMCS parameter (Equation (3)) was computed for all points in the crack-front neighborhood; and, 3) a multiple specimen *R*-curve was used to define the point of fracture initiation. The sections below describe in some detail the influence of each of these choices on the resulting fracture predictions.

8.1 Use of Companion Modeling to Understand Tensile Specimen Behavior

Companion modelling was used to determine the state of stress and strain in notched tensile specimens. Tensile behavior has often been interpreted in the literature using semi-empirical relations. Despite its poor description of the actual state of stress and strain in the notched tensile specimens (as evidenced by the data in Figure 8), fracture prediction using the semi-empirical critical plastic strain correlation of Figure 9 provides a comparison between previously published work and the results presented here. The semi-empirical correlation results for both the long- and short-crack geometries are labeled "Semi-empirical" in Figure 17 (predictions labeled "θ = 0" are described below). The calibrated length scale from the semi-empirical correlation is 0.0013W, about one-fifth that obtained above. The corresponding toughness results for the long- and short-crack specimens are $J/(B\sigma_o) = 1.65\cdot10^{-3}$ and $1.68\cdot10^{-3}$, respectively. Therefore, using the semi-empirical correlation predicts a toughness elevation of only 2.1% for the short-crack specimen. This result is consistent with the experimental trends shown in Figure 17; however, it does not reflect the usual experimental measurements showing short cracks having higher toughness.

8.2 Examination of the Crack-tip Region

The work presented here examines the entire crack tip region to find the point closest to failure. Previous studies have evaluated critical plastic strain directly ahead of the crack tip (i.e., taking $\bar{\theta} = 0$ in Equation (3)) [*4*][*24*]. In this study, SMCS was first satisfied on $\bar{\theta} = \pi/4$ for both crack geometries. Restricting the scope of the assessment to $\bar{\theta} = 0$ results in a smaller calibrated length scale, as shown by the point labeled "θ = 0" in Figure 17(a). The resulting prediction for the short-crack geometry, labeled "θ = 0" in

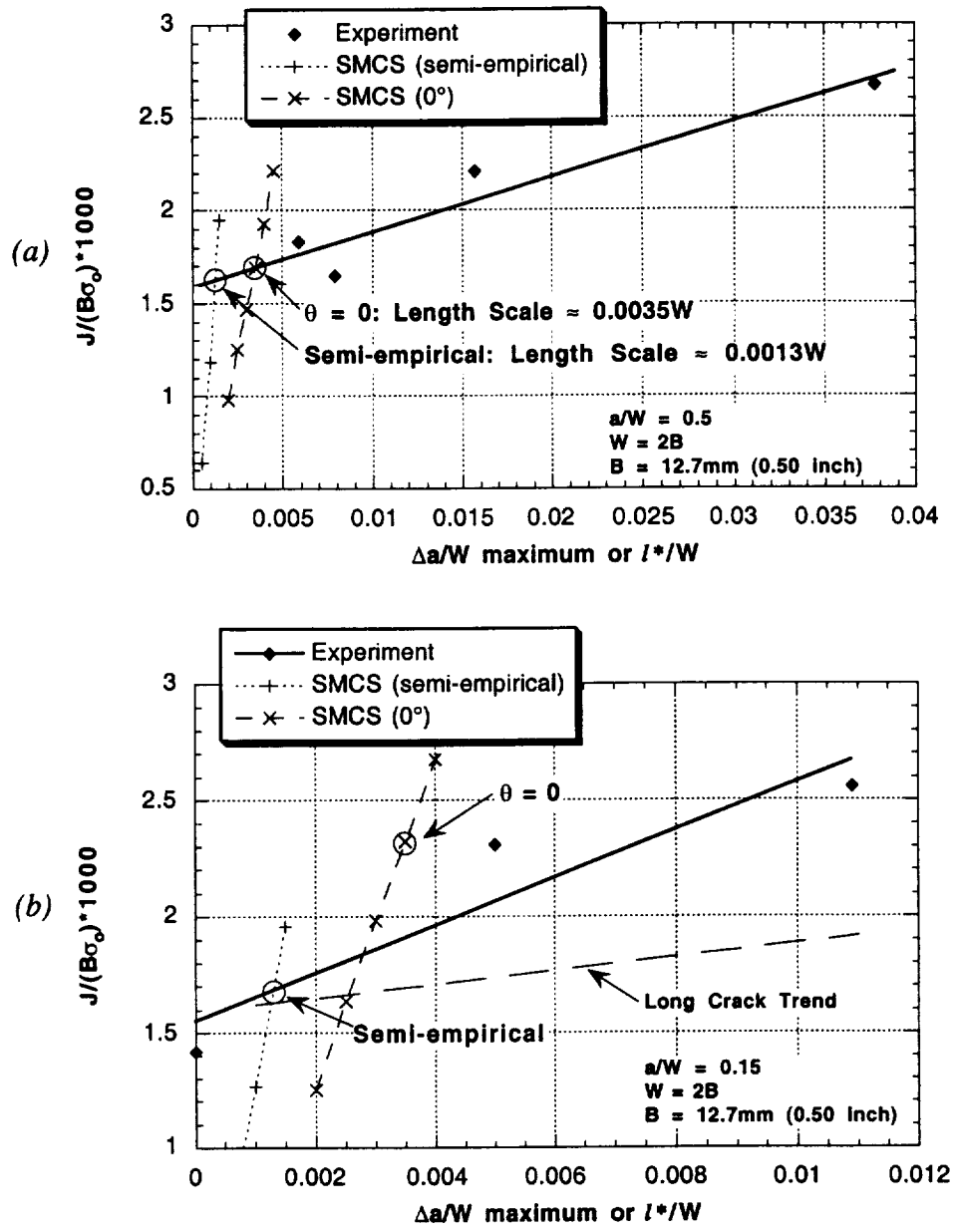

Figure 17. SMCS criterion derived from semi-empirical tensile data and from taking $\bar{\theta} = 0$: *(a)* Calibration of length scale using long-crack data, *(b)* short-crack prediction and experimental crack-growth data.

Figure 17(b), is above the experimental trend. Previous work has shown that under varying conditions of constraint and toughness, the SMCS criterion will be satisfied at different angular orientations. Here we find $\bar{\theta} = \pi/4$ in both specimen types, but Panontin, et al, found $\bar{\theta} = 0$ for a variety of specimens [*15*]; however, the materials in [*15*] were significantly different than aluminum, being of higher toughness (by as much as an order of magnitude) and exhibiting greater strain hardening. The fractographic evidence in this study (Figure 10) suggests that failure first initiates at an oblique angle and then propa-

gates by microcracking between growing voids. Including the possibility of initiation at an oblique angle, then, is also in keeping with the physical phenomenon being modeled.

8.3 Consistent Determination of Tearing Onset

Accurate measurement of crack extension is critical in the calibration and qualification of the SMCS approach. The work presented here uses a multiple specimen R-curve to quantify tearing near initiation, over a range of conditions. Other authors have used standardized fracture measures, such as K_{Ic} or J_{Ic}, to calibrate the length scale [4][24]. Further, J_{Ic} measurements are often based on unloading compliance. In the following, we revisit the experimental results to investigate the efficacy of using standard toughness measures in place of the interrupted test results.

By interrupting the fracture tests near the onset of tearing in this study, the amount of tearing was accurately determined. A scanning electron microscope was used to measure the maximum amount of tearing on the failed specimen surface. Because of material and stress-state variations along the crack-front, tearing was non-uniform in all specimens (i.e., crack tunneling was observed). Therefore one would not expect the SEM crack length measurements to agree with results of unloading compliance. Crack extension from SEM measurements and from unloading compliance are given in Table 3 for the long-crack specimens. Here we see that the compliance technique underestimates the maximum amount of tearing. Optical microscopy results are also given in Table 3, where measurements were performed at 9 points along the crack front as specified in ASTM E-1152. The compliance and optical estimates of average crack extension do not agree. In fact, unloading compliance underestimates crack extension by a factor of two. A number of other R-curve studies comparing multiple-specimen and key-curve methods with unloading compliance also indicate its tendency to drastically underestimate crack extension near initiation [25][26][27]. Therefore, to be consistent with a micromechanical definition of fracture initiation, a multiple specimen R-curve is apparently needed for length scale calibration.

Specimen	*SEM*	*Compliance*	*Optical Microscopy*	
	$\Delta a/W$ max	*$\Delta a/W$*	*$\Delta a/W$ (9-pt. avg.)*	*$\Delta a/W$ max*
14TL	0.0157	0.003	0.006	0.015
15TL	0.0079	0.000	0.000	0.000
18TL	0.0378	0.011	0.020	0.042
19TL†	0.0060	0.000	—	0.006

Table 3. Comparison of crack length measurements resulting from various techniques.

† Specimen 19TL was not fatigued post-test. Instead, the un-failed specimen was sectioned in the S-W plane (Figure 1) and incrementally polished to find the plane of maximum tearing.

Various, average toughness measures for the long- and short-crack specimens are summarized in Table 4. Long-crack, single specimen toughness from the linear fit to J-Δa unloading compliance data (Figure 16) differs from the multiple specimen result (Figure 11) by 32% (2.34 compared to 1.77). This is the case even though both are evalu-

Geometry	$J/(B\sigma_o)*1000$		
	Multiple Specimen	Single Specimen, from J_Q (Linear)	Single Specimen, from J_{KQ} (E-399)
$a/W = 0.5$	1.77	2.34	2.16
$a/W = 0.15$	2.16 (22%)	--	2.65 (23%)

Table 4. Comparison of average measured toughness for long- and short-crack specimens (values in parenthesis indicate percent change from long-crack value).

ated at $\Delta a/W = 0.006$. This discrepancy is due both to the difference between *maximum* and *average* definitions of crack growth and the inaccuracy of unloading compliance. Long- and short-crack values of J_{KQ} are also shown in Table 4, and both reflect a significant elevation in toughness above that defined using the multiple specimen approach. Nevertheless, the J_{KQ} results indicate a 23% toughness increase for the short crack specimens (2.16 compared to 2.65), which is the very similar to the 22% change indicated by multiple-specimen, interrupted testing.

Based on these results, it appears that percentage comparisons of constraint effects in similar specimens can be made using either interrupted testing or E-399. This appears true even though these two toughness measures vary by as much as 23% for the same specimen (2.16 compared to 2.65 for $a/W = 0.15$). Since either measure indicates the same percent toughness elevation, one might conclude that the specimen R-curves are changing in proportion for small amounts of crack extension. However, while toughness for both specimen types was found at $\Delta a/W = 0.006$ (maximum) for the interrupted specimens, tearing is not the same at J_{KQ} in the non-interrupted specimens. Using the trendlines in Figures 11 and 12, we can approximate the maximum tearing present in the long- and short-crack specimens at their respective values of J_{KQ}. Doing so indicates that $\Delta a/W = 0.019$ and 0.011 at J_{KQ} for the long- and short-crack specimens, respectively. This suggests that the slope of the R-curve is steeper for short-crack specimens, which follows both conventional wisdom and the trend in the data shown in Figure 12. In summary, the data suggest that the percent change in toughness from one specimen type to another, evidenced by single specimen R-curves and by the global measure J_{KQ}, are in agreement.

Several of the choices made in reducing, combining, and presenting the computational results and experimental data of this study have important influences on the results. Given the data presented above, the use of standard toughness measures to define the length scale separates the link between Δa and l^* assumed when invoking a micromechanical approach. Compounding the effects of defining initiation toughness based on E-399, for example, while making use of semi-empirical data reduction for tensile specimens, the length scale and tearing at "initiation" differ by a factor of 14 ($l^*/W = 0.0013$ and $\Delta a/W = 0.019$). Such an approach, then, is inconsistent with the processes at work on the microscale and calls into question the assertion of a micromechanical methodology. In contrast, the use of a multiple specimen R-curve allows consistent micromechanical calibration of the length scale. Once calibrated, the data suggest that micromechanical predictions of constraint-induced toughness change can be used to predict changes in global fracture measures such as J_{KQ}.

9. Conclusions

The following are the major conclusions of this study:

- Companion modeling of tensile specimens produced significantly different estimates of plastic strain and triaxiality compared with semi-empirical formulae
- Equivalent plastic strain at fracture decreases exponentially with stress triaxiality in 7050-T7451
- The length scale for fracture can be defined at the intersection of the computational J-l^* curve and the experimental J-R curve
- SMCS model parameters for 7050-T7451 in the TL orientation were found to be $\alpha = 4.2$, $\beta = 3.7$, and $l^* = 0.15$ mm (0.0060 in)
- In crack geometries, the SMCS fracture criterion was first satisfied oblique to the cracking direction (i.e., at $\bar{\theta} = \pi/4$), on the specimen midplane
- The SMCS approach produced accurate fracture assessment over the constraint range $-0.22 \leq Q \leq 0$
- Percent changes of toughness predicted by SMCS agreed with percent changes in J_{KQ} determined from E-399
- Because standard toughness measures correspond to crack extensions significantly larger than the calibrated length scale, they are inappropriate for use in length scale calibration

10. Acknowledgments

Funds for the support of this study have been allocated by the NASA-Ames Research Center, Moffett Field, California, under Interchange No. NCC2-5214. Thanks to Theodore Yau for performing much of the mechanical testing, and to Kyle Hukari for data reduction.

11. References

[1] Panontin, T. L. and Hill, M. R., "The effect of residual stresses on brittle and ductile fracture initiation predicted by micromechanical models," *International Journal of Fracture*, Vol. 82, 1996, pp. 317-333.

[2] O'Dowd, N. P. and Sumpter, J. D. G., "Effect of thermomechanical loading on near tip constraint," *Journal De Physique IV*, Vol. 6, No. NC6, 1996, pp. 539-548.

[3] Hill, M. R. and Yau, T., "Triaxial residual stresses affect driving force and constraint to alter fracture toughness," *The Sixth International Conference on Residual Stresses*, The Institute of Materials, Oxford, UK, 2000, pp. 1485-1492.

[4] Mackenzie, A. C., Hancock, J. W. and Brown, D. K., "On the influence of state of stress on ductile failure initiation in high strength steels," *Engineering Fracture Mechanics*, Vol. 9, No. 1, 1977, pp. 167-188.

[5] *Metallic Materials and Elements for Aerospace Vehicle Structures (MIL-HDBK-5G)*, US Department of Defense, Washington, D.C., 1994.

[6] ASTM, "Standard E1152-87: Test Method for Determining J-R Curves," American Society for Testing and Materials, Philadelphia, PA, 1987.

[7] Schwalbe, K.-H., "On the influence of microstructure on crack propagation mechanisms and fracture toughness of metallic materials," *Engineering Fracture Mechanics*, Vol. 9, 1977, pp. 795-832.

[8] Hancock, J. W. and Mackenzie, A. C., "On the mechanisms of ductile failure in high-strength steels subjected to multi-axial stress-states," *Journal of the Mechanics and Physics of Solids*, Vol. 24, No. 2/3, 1976, pp. 147-169.

[9] Panontin, T. L., "The relationship between constraint and ductile fracture initiation as defined by micromechanical analyses," Ph.D., Stanford University, 1994.

[10] Hancock, J. W. and Cowling, M. J., "Role of state of stress in crack-tip failure processes," *Metal Science*, Vol. 14, No. 8-9, 1980, pp. 293-304.

[11] *ABAQUS/Standard, Version 5.8*, Hibbitt, Karlsson, and Sorenson, Inc., Providence, RI, 1999.

[12] Gullerud, A. S., Koppenhoefer, K. C., Roy, A. and Dodds, R. H., "WARP3D: 3-D Dynamic Nonlinear Fracture Analysis of Solids Using Parallel Computers and Workstations," Structural Research Series 607, Univ. of Illinois, 2000.

[13] Anderson, T. L., *Fracture mechanics: fundamentals and applications*, 2nd ed., CRC Press, Boca Raton, 1995.

[14] Dowling, N. E., *Mechanical behavior of materials: engineering methods for deformation, fracture, and fatigue*, 2nd ed., Prentice Hall, Upper Saddle River, NJ, 1999, page 128.

[15] Panontin, T. L. and Sheppard, S. D., "Experimentally verified finite element study of the stress-strain response of crack geometries experiencing large-scale yielding," *ASTM STP 1296*, ASTM, West Conshohocken, PA, 1997, pp. 216-242.

[16] Panontin, T. L. and Sheppard, S. D., "Relationship between constraint and ductile fracture initiation as defined by micromechanical analyses," *ASTM STP 1256*, ASTM, West Conshohocken, PA, 1995, pp. 54-85.

[17] Gao, X. S., Faleskog, J. and Shih, C. F., "Cell model for nonlinear fracture analysis - II. Fracture-process calibration and verification," *International Journal of Fracture*, Vol. V89, No. N4, 1998, pp. 375-398.

[18] O'Dowd, N. P. and Shih, C. F., "Family of Crack-Tip Fields Characterized by a Triaxiality Parameter: Part I-Structure of Fields," *Journal of the Mechanics and Physics of Solids*, Vol. 39, 1991, pp. 989-1015.

[19] O'Dowd, N. P. and Shih, C. F., "Family of Crack-Tip Fields Characterized by a Triaxiality Parameter: Part II-Fracture Applications," *Journal of the Mechanics and Physics of Solids*, Vol. 40, 1992, pp. 939-963.

[20] O'Dowd, N. P. and Shih, C. F., "Two-parameter fracture mechanics: theory and applications," *Fatigue and Fracture Mechanics: 24th Volume, ASTM STP 1207*, J. D. Landes, D. E. McCabe and J. A. M. Boulet, Eds., ASTM, Philadelphia, 1995, pp. 21-47.

[21] Bridgman, P. W., *Studies in large plastic flow and fracture with special emphasis on the effects of hydrostatic pressure*, McGraw Hill, New York, 1952.

[22] ASTM, "Standard E813-89: Test Method for J_{IC}, A Measure of Fracture Toughness," American Society for Testing and Materials, Philadelphia, PA, 1989.

[23] ASTM, "Standard E399-90: Test method for plain-strain fracture toughness of metallic materials," American Society for Testing and Materials, Philadelphia, PA, 1990.

[24] Haynes, M. J., Somerday, B. P., Lach, C. L. and Gangloff, R. P., "Micromechanical modeling of temperature-dependent initiation fracture toughness in advanced aluminum alloys," *ASTM STP 1297*, ASTM, West Conshohocken, PA, 1997, pp. 165-190.

[25] Joyce, J. A., Ernst, H. and Paris, P. C., "Direct Evaluation of J-Resistance Curves from Load Displacement Records," *Fracture Mechanics: Twelfth Conference, ASTM STP 700*, American Society for Testing and Materials, 1980, pp. 222-236.

[26] John, S. J., "Obtaining J-Resistance Curves Using the Key-Curve and Elastic Unloading Compliance Methods: An Integrity Assessment Study," *Elastic-Plastic Fracture Test Methods; The User's Experience (Second Volume), ASTM STP 1114*, American Society for Testing and Materials, Philadelphia, 1991, pp. 133-149.

[27] Ohtsuka, N., "Nonincremental Evaluation of Modified J-R Curve," *Elastic-Plastic Fracture Test Methods; The User's Experience (Second Volume), ASTM STP 1114*, American Society for Testing and Materials, Philadelphia, 1991, pp. 150-162.